1 Methods

1.1 Electrophysiological recordings

1.1.1 Chronic microdrive array experiments

Three Long-Evans male rats, 3-6 months old, were chronically implanted with custom microdrive arrays targeting rectangular grids in field CA1 of the hippocampus and allowing the independent depth adjustment of 24 tetrodes and 4 single electrodes. In all three grids the probe spacing was 0.5 mm and the target anatomical position of the caudomedial grid corner was bregma = -5.3 mm, lateral = 1.0 mm. The rostrocaudal vs. mediolateral grid dimensions were 6x5, 4x8, and 5x6 (Fig. S3). Following recovery from surgery the experiments proceeded in two phases (Fig. S1).

In **phase one**, tetrodes were slowly lowered (in 5-6 days) to stratum oriens of CA1. This was accomplished by the following methodology. First, the target depth of each tetrode was computed based on an atlas of the rat brain in stereotaxic coordinates [1, 2]. Every adjustment was logged and compared against the expected target depth. Second, electrophysiological criteria were continuously monitored online to infer the relative locations of tetrode tips with respect to different brain landmarks. In particular, exiting corpus callosum and entering stratum oriens of CA1 was signaled by the increase in spiking chatter and the appearance of sharp waves (SPW) of positive polarity. Further approaching the pyramidal cell layer was invariably associated with an increase in SPW-associated ripple power. Tetrodes were deemed to be in stratum oriens of CA1 if the following criteria were met: the adjustment log indicated that tetrodes were near the target depth; sharp-waves, when visible, were of positive polarity; the depth of the CA1 pyramidal cell layer, as signaled by the presence of high-amplitude (> 500 μV) complex spiking activity, had not been reached yet. We emphasize that all depth adjustments were blind with respect to wave propagation analysis, which was only carried out after each animal had already been euthanized. Once all tetrodes were in stratum oriens of CA1, 3-4 recording sessions were obtained while rats ran for $\sim$ 45 min on a 180 cm linear track for water reward delivered at each end (Fig. S1a). Data were usually also recorded for several hours before and after, while rats rested or slept in a small rectangular box near the linear track.

In **phase two**, tetrodes were further lowered to the CA1 pyramidal cell layer and micro-adjusted to maximize single unit isolation. During this phase, a few electrodes inadvertently traveled to depths in stratum radiatum. In these cases, the tetrodes were retracted in search of CA1 units. Once unit activity was present on the majority of the tetrodes, recording sessions were obtained as in phase one (Fig. S1b). In particular, the wide band, 1-9000 Hz, differential signal from all 100 channels was amplified by a gain of 2000, sampled at 25 KHz, digitized with 24 bit resolution and stored to disk for off-line analysis using custom data acquisition software. Two skull screws implanted above the ipsilateral cerebellum and the contralateral cortex served as ground and reference, respectively.

At the conclusion of each experiment, a lethal pentobarbital (100 mg/kg) injection was administered and the final anatomical location of each tetrode was marked by an electrolytic lesion (10 μA anodal current for 15 sec). The animal was then transcardially perfused first with saline and then with 4% paraformaldehyde solution in PBS. After the brain was fixed, electrodes were retracted, the brain was extracted, and a high resolution structural MRI scan was performed to reconstruct electrode tracks in 3D (Fig. S1c).

1.1.2 Acute multisite silicon probe experiments

Two Long-Evans male rats, 3-6 months old, were anesthetized with urethane (1.3 g/kg) and placed in a stereotactic apparatus. A 1-2 mm^2 craniotomy was performed centered at bregma = -3.9 mm, lateral = 2.7 mm. The dura was removed and a multisite silicon probe (NeuroNexus Technologies, Probe 2b, 54 sites in 2 staggered columns 43 μm apart, 50 μm vertical site spacing within each column) was stereotactically lowered so that the middle of its recording vertical extent was approximately at the CA1 pyramidal cell layer. Data were acquired as above throughout the 8-10 hour duration of the experiments, which included periods of spontaneous or pinch-induced theta, as well as spontaneous sharp-wave/ripple events.

1.1.3 Chronic multisite silicon probe experiments

Two Long-Evans male rats, 3-6 months old, were chronically implanted with mutlisite silicon probes (NeuroNexus Technologies, Probe 2b) targeting bregma = -3.9 mm, lateral = 2.7 mm. During surgery the probes were stereotactically lowered so that the middle of the recording vertical extent was approximately at the CA1 pyramidal cell layer and then cemented to the skull. Two skull screws implanted above the contralateral cerebellum and cortex served as ground and reference, respectively. Following 3-4 days of recovery time after surgery, recordings from one site column (25 sites with 50 μm vertical spacing; the two deepest sites were not recorded because reference signals were fed through their corresponding channels) were obtained as rats ran and slept in the same environments as in the microdrive array experiments.

1.2 Electrode position reconstruction

The actual anatomical locations of the recording electrodes were analyzed in two ways. First, tetrode tracks and the final positions of tetrode tips at the conclusion of experimental phase 2 were localized by high resolution structural MRI (Fig. S1c, S18). Figures S19-S27 show high magnification MRI coronal sections for each row in the 4x8 and the 5x6 grids. The insets show full MRI coronal sections around the magnified ones. The section numbers are shown in the upper left corners of the insets (consecutive sections are ~ 70 μm apart; section 1 corresponds to different bregma coordinates in the two animals). The MRI data demonstrate that electrodes indeed reached CA1 in a grid arrangement. In the 4x8 and 5x6 arrays the two electrodes at the caudomedial corner may have been in subiculum (as marked in Fig. 3, S21, S22, S26, S27). The MRI data also show that at the conclusion of phase 2 all electrodes (except the ones mentioned above and the most

lateral one marked in Fig. S22–all excluded from unit analysis) were in area CA1. Second, sharp-wave polarity analysis was used to confirm that all tetrodes were in stratum oriens above CA1 for data recorded during phase 1 (Fig. S1a, section 1.2.2).

1.2.1 Structural MRI scans

Anatomical three dimensional images were obtained from a 7 Tesla Bruker Biospec Horizontal Bore Small Animal Imaging System (Bruker, Karlsruhe, Germany) using a Rapid Acquisition with Relaxation Enhancement (RARE) sequence with the following parameters: TR/TE = 600/10 (ms), RARE factor = 8, averages = 26, total imaging time $\approx$ 32 (hr), raw spatial resolution = 85 (μm^3). Before initiating the imaging the fixed brain specimens were treated as described in [3]. The immersion in a gadoteridol solution allows for a significant reduction in the intrinsic T1 value of the sample and therefore reduces the total imaging time for a given resolution and target signal to noise.

1.2.2 Sharp-wave analysis

Sharp-wave/ripple (SWR) events were detected based on ripple power during run sessions and their flanking sleep sessions. In particular, the broadband signal from each channel was filtered between 80-250 Hz (Parks-McClellan optimal equiripple FIR filter, 80-250 Hz pass band, 50-80 Hz and 250-280 Hz transition bands, 40 dB minimum attenuation in the stop bands) and candidate SWR events were identified as deviations in the power of the filtered traces exceeding 2 standard deviations. Candidate events shorter than 20 ms or of mean frequency below 100 Hz were rejected. SWRs were identified as candidate events simultaneously detected across multiple tetrodes or silicon probe sites in the proximity of the CA1 cell layer. The centers of SWR events were used as triggers for averaging the lowpass filtered (Parks-McClellan optimal equiripple FIR filter, 14-16 Hz transition band, 40 dB minimum attenuation in the stop band) signal on each channel, thus giving the mean sharp-wave (SPW) at each tetrode or silicon probe site (Fig. S4). The amplitude of the SPW was measured at the time offset (-8.8 ms mean) corresponding to the SPW waveform peak.

Analysis of the chronic mutlisite probe experiment data (Fig. S4d) demonstrates that SPWs are of positive polarity throughout the depth of stratum oriens and reverse polarity abruptly at or slightly below the CA1 pyramidal cell layer, consistent with previous data [4]. Analysis of the tetrode grid data (Fig. S4a-c) obtained during phase 1 demonstrates that the SPWs on all tetrodes are of positive polarity and therefore all tetrodes were no deeper than stratum oriens of CA1 as intended. Notice that panels a-c in Figure S4 are based on data immediately adjacent to the data presented in panels a-c of Figure 3.

1.3 LFP theta wave analysis

Let $\mathbf{x} = (x, y, z)$ specify a point in the brain, where x is mediolateral, y rostrocaudal (bregma), and z dorsoventral coordinate. Wide band signals were recorded at points $\mathbf{x}$, anti-aliased and downsampled to 208.33 Hz, and then theta filtered (Parks-McClellan optimal equiripple FIR filter, 4-10 Hz pass band, 3-4 Hz and 10-11 Hz transition bands,

40 dB minimum attenuation in the stop bands) to give narrow band theta signals $u(\mathbf{x},t)$ at each point. To obtain the instantaneous amplitude ρ, and phase φ, of theta oscillations the analytic signal was computed

$$u_a(\mathbf{x},t) = u(\mathbf{x},t) + j \cdot u_h(\mathbf{x},t) = \rho(\mathbf{x},t)e^{j\varphi(\mathbf{x},t)} \tag{1}$$

where $u_h(\mathbf{x},t)$ is the Hilbert transform of $u(\mathbf{x},t)$ and $j = \sqrt{-1}$. Instantaneous theta amplitude and phase were obtained from the analytic signal as

$$\rho(\mathbf{x},t) = |u_a(\mathbf{x},t)| \tag{2}$$
$$\varphi(\mathbf{x},t) = \arg(u_a(\mathbf{x},t)) \tag{3}$$

The instantaneous theta angular frequency was obtained as the time derivative of the unwrapped phase

$$\omega(\mathbf{x},t) = \dot{\varphi}(\mathbf{x},t) \tag{4}$$

How does the phase of theta oscillations depend on anatomical coordinates? If theta oscillations were synchronized with zero lag across the hippocampus, then

$$\varphi(\mathbf{x},t) = \omega t + \phi_{\mathbf{x}}(z) \tag{5}$$

where ω is the angular theta frequency and $\phi_{\mathbf{x}}(z)$ gives the dependence of theta phase on depth through point $\mathbf{x}$. Exploratory data analysis indicated that the phase of theta may also depend approximately linearly on the other two coordinates, i.e.

$$\begin{aligned}\varphi(\mathbf{x},t) &= \omega t - k_x x - k_y y + \phi_{\mathbf{x}}(z) \\ &= \omega t - \mathbf{k}\cdot\mathbf{x} + \phi_{\mathbf{x}}(z)\end{aligned} \tag{6}$$

where $\mathbf{k} = (k_x, k_y, k_z)$ is the wave vector. Notice that by definition $k_z = 0$ and the dependence of theta phase on depth is completely specified by $\phi_{\mathbf{x}}(z)$. When $\mathbf{k} = 0$ eq. 6 reduces to the synchronized case (eq. 5), so to choose between the two models we need to test the hypothesis $H_1 : \mathbf{k} \neq 0$ against the null alternative $H_0 : \mathbf{k} = 0$. In order to proceed we need the form of $\phi_{\mathbf{x}}(z)$, which was experimentally determined as follows.

Using a mutlisite silicon probe theta was recorded at points $\mathbf{x}_i$, such that $x_m = x_n$, $y_m = y_n$, and $z_m - z_n = (m-n)dz$, where $dz = 50$ μm and $0 \leq m, n \leq 26$. Since the x and y coordinates of all recording locations are the same, from eq. 6

$$\phi_{\mathbf{x}}(z_i) = \langle \varphi(\mathbf{x}_i,t) - \varphi(\mathbf{x}_0,t) \rangle + \phi_0 \tag{7}$$

where $\langle\cdot\rangle = \frac{1}{T}\sum_t \cdot$ denotes a time average and $\phi_0 = \phi_{\mathbf{x}}(z_0) = \text{const}$. Since the theta phases in the brackets are experimentally measured quantities, $\phi_{\mathbf{x}}(z)$ is determined up to the constant ϕ_0, while its vertical (dorsoventral) gradient is completely specified

$$\frac{\partial \phi_{\mathbf{x}}(z_i)}{\partial z} = \frac{\phi_{\mathbf{x}}(z_{i+1}) - \phi_{\mathbf{x}}(z_i)}{dz} \tag{8}$$

Experimentally the dorsoventral phase gradient was measured to be zero above the pyramidal cell layer of CA1, i.e. $\partial\phi_{\mathbf{x}}(z)/\partial z = 0$ for $z < z_p(x,y)$, where $z_p(x,y)$ denotes the

depth of the cell layer below (x, y). Therefore, above the cell layer eq. 7 reduces to $\phi_{\mathbf{x}}(z) = \phi_0 = \text{const}$ and from eq. 6 theta oscillations in stratum oriens above CA1 can be described as

$$\varphi(\mathbf{x}, t) = \omega t - \mathbf{k} \cdot \mathbf{x} + \phi_0 \tag{9}$$

with $\mathbf{k} = 0$ in the case of zero lag synchronization.

The wave vector $\mathbf{k}$ was measured as follows. Using a tetrode array theta was recorded at points $\mathbf{x}_{mn}$, $1 \leq m \leq M$, $1 \leq n \leq N$, arranged as a rectangular grid in stratum oriens of CA1, i.e. $x_{mn} - x_{pq} = (n-q)dx$, $y_{mn} - y_{pq} = (p-m)dy$, $z_{mn} < z_p(x_{mn}, y_{mn})$, with spacing $dx = dy = 0.5$ mm. Let $\mathbf{x}_{pq}$ be the point approximately in the center of the grid, i.e. $p = \lceil M/2 \rceil$, $q = \lceil N/2 \rceil$, and define the theta phase deviations

$$\begin{aligned} \Delta\varphi_{ij}(t) &= \varphi(\mathbf{x}_{pq}, t) - \varphi(\mathbf{x}_{ij}, t) \\ &= \mathbf{k} \cdot \mathbf{x}_{ij} - \mathbf{k} \cdot \mathbf{x}_{pq} \\ &= k_x x_{ij} + k_y y_{ij} - k_0 \end{aligned} \tag{10}$$

where $k_0 = \mathbf{k} \cdot \mathbf{x}_{pq}$ is a constant term determined by the arbitrary choice of the reference point $\mathbf{x}_{pq}$. Equation 10 defines a linear multiple regression model, with the theta phase deviations $\Delta\varphi_{ij}(t)$ being the response variable and the coordinates x_{ij}, y_{ij}, being the explanatory variables. At each time point 24 to 28 phase deviations $\Delta\varphi_{ij}(t)$ were measured allowing the wave vector $\mathbf{k}(t)$ to be estimated by least squares. The null hypothesis of zero lag synchronization corresponds to $\mathbf{k}(t) = 0$ and was therefore tested at each time point using ANOVA for multiple regression. The general applicability of the linear model was confirmed by examining the residuals and the coefficient of determination. The null hypothesis was also tested by subjecting the averaged phase deviations $\langle \Delta\varphi_{ij}(t) \rangle$ to multiple regression analysis as above. Rejecting the null hypothesis in this case also requires that the wave vector shows consistent behavior over time.

The form of equation 9 specifies a traveling plane wave. Given the angular frequency $\omega(t)$ and the wave vector $\mathbf{k}(t)$, the instantaneous frequency $f(t)$, spatial wavelength $\lambda(t)$, phase velocity $v(t)$, and propagation direction $\theta(t)$ are given by the standard equations

$$f(t) = \omega(t)/(2\pi) \quad (\text{Hz}) \tag{11}$$

$$\lambda(t) = (2\pi)/\|\mathbf{k}\| \quad (\text{mm}) \tag{12}$$

$$v(t) = f(t)\lambda(t) \quad (\text{mm/s}) \tag{13}$$

$$\theta(t) = \arg(k_x + jk_y) \quad (\text{rad}) \tag{14}$$

1.3.1 Ranges of theta phase-shifts across the recording arrays

The expected maximum instantaneous phase shift (in degrees) across the array is:

$$d\varphi_e = 360\frac{dx}{\lambda} \tag{15}$$

where dx is the span of the recording array along the direction of wave propagation and λ is the spatial wavelength (eq. 12). If $d\varphi_o$ denotes the actual observed median maximum instantaneous phase shift and $d\langle\Delta\varphi\rangle$ denotes the maximum mean phase shift across the

recording array, the values of these quantities for the datasets reported in Fig. 3 are:

array	dx (mm)	λ (mm)	$d\varphi_e$ (deg)	$d\varphi_o$ (deg)	$d\langle\Delta\varphi\rangle$ (deg)
6x5	2.5	13.6	66	87	43
4x8	3.5	10.8	117	124	75
5x6	2.0	14.4	50	68	66

Notice that $d\langle\Delta\varphi\rangle$ may be considerably smaller than the expected and observed maximum instantaneous phase shifts, because it is the difference between time-averaged quantities and therefore fluctuations in the instantaneous values of wave parameters reduce its magnitude.

The extrapolated maximum instantaneous phase difference across CA1 is obtained from equation 15 after setting $dx = l$, where $l \approx 10$ (mm) is the length of the septotemporal axis of CA1. Our data places λ in the range between 10 and 15 (mm) corresponding to an extrapolated phase difference between 240 and 360 degrees, i.e. two thirds to a full theta cycle.

1.4 Spiking wave analysis

Spiking analysis overview

The analysis objective is to test the hypothesis that spiking in CA1 is organized as a traveling wave against the null alternative that peak firing is synchronized across the hippocampus. The idea is to compute the mean phase of firing of the local neuronal population recorded at each point of the grid with respect to a single arbitrary theta reference LFP. Under the null hypothesis of synchrony the mean phase of firing at each point of the grid should be identical–the precise value will of course depend on the anatomical location of the theta reference. Alternatively, if spiking is organized as a traveling wave, the mean phase of firing should systematically advance across the grid in the direction of wave propagation.

Can the spiking wave be measured instantaneously? We recorded the spiking activity of multiple neurons in CA1 while rats ran on a linear track (Fig. S6, S8, S9). Over the timescale of a minute, the pattern of neuronal activity appears dense and reproducible across laps (Fig. S6a, S8a, S9a), but a closer look reveals how sparse firing actually is within individual theta cycles (Fig. S6b, S8b-e, S9b-e). This sparseness necessitates averaging activity across theta cycles, i.e. performing theta phase-locking analysis (Fig. S6d-e, S12, S13). The latter reveals how firing probability is modulated for each neuron (Fig. S6d, S10, S12), each local neuronal population (Fig. S6e-f, S13), and across the recording array (Fig. S6g-i, S14).

Spiking analysis details

Using a tetrode array spiking was recorded at points $\mathbf{x}_{mn}$, $1 \le m \le M$, $1 \le n \le N$, arranged as a rectangular grid in the pyramidal cell layer of CA1, i.e. $x_{mn} - x_{pq} = (n - q)dx$, $y_{mn} - y_{pq} = (p - m)dy$, $z_{mn} = z_p(x_{mn}, y_{mn})$. Let τ_{kl} be the time of the l^{th} spike,

out of N_k total, fired by the k^{th} unit recorded at anatomical location $\mathbf{x}_k$. Let $\mathbf{x}_{pq}$ be the point approximately at the center of the recording grid. Then $\varphi(\mathbf{x}_{pq}, t)$ is the reference phase of theta with respect to which all phase-locking analysis is performed. The mean phase μ_k and mean resultant length $\bar{R}_k$ corresponding to unit k are obtained from the first trigonometric moment

$$m_k^{'} = \frac{1}{N_k} \sum_{l=1}^{N_k} e^{j\varphi(\mathbf{x}_{pq}, \tau_{kl})} = \bar{R}_k e^{j\mu_k} \tag{16}$$

The significance of theta phase locking for each unit was determined using the Rayleigh statistic $Z_k = N_k \bar{R}_k^2$ after correcting for theta waveform asymmetry [5]. Let $U_{\mathbf{x}}$ be the set of all significantly theta phase-locked units recorded at anatomical location $\mathbf{x}$. The population mean phase $\mu(\mathbf{x})$ was obtained from the first trigonometric moment

$$m(\mathbf{x})^{'} = \frac{1}{|U_{\mathbf{x}}|} \sum_{k \in U_{\mathbf{x}}} e^{j\mu_k} = \bar{R}(\mathbf{x}) e^{j\mu(\mathbf{x})} \tag{17}$$

When spikes at each grid location were combined into a multiunit, instead of being partitioned into multiple single units, eq. 16 yields the multiunit mean phase. In this case the population mean phase $\mu(\mathbf{x})$, defined in eq. 17, reduces to the multiunit mean phase from eq. 16. Notice that the population mean phase weighs all neurons equally, while the multiunit mean phase weighs all spikes equally. In practice both measures yield very comparable results (Fig. S6g,h).

What is the expected behavior of $\mu(\mathbf{x}_{ij})$? Under the null hypothesis of synchronous firing $\mu(\mathbf{x}_{ij})$ is constant. Alternatively, the spiking wave hypothesis is based on the assumption that the mean phase of CA1 spiking with respect to theta oscillations recorded locally, in stratum oriens above the pyramidal cell layer, is a constant μ_0 independent of septotemporal and transverse coordinates. Since $\mu(\mathbf{x}_{ij})$ is computed with respect to a non-local reference

$$\mu(\mathbf{x}_{ij}) = \mu_0 + \langle \Delta\varphi_{ij}(t) \rangle + \epsilon \tag{18}$$

where $\langle \Delta\varphi_{ij}(t) \rangle$ accounts for the mean phase deviation between the local and the reference theta oscillation in stratum oriens, while ϵ is an offset determined by the depth from which the reference theta oscillation is recorded. Define the spiking mean phase deviations

$$\begin{aligned} \Delta\mu_{ij} &= \mu(\mathbf{x}_{ij}) - \mu(\mathbf{x}_{pq}) \\ &= \langle \Delta\varphi_{ij}(t) \rangle - \langle \Delta\varphi_{pq}(t) \rangle \\ &= \langle \Delta\varphi_{ij}(t) \rangle - 0 \\ &= k_x x_{ij} + k_y y_{ij} - k_0 \end{aligned} \tag{19}$$

where the second line is obtained after substituting eq. 18 in the definition and the final line is obtained after substituting eq. 10 under the assumption that the theta wave vector $\mathbf{k}$ does not depend on time. Equation 19 defines a linear regression model similar to eq. 10, but with the spiking mean phase deviations $\Delta\mu_{ij}$, rather than the theta phase deviations $\Delta\varphi_{ij}(t)$, being the response variable. The spiking wave hypothesis $H_1 : \mathbf{k} \neq 0$

was tested against the null alternative $H_0 : \mathbf{k} = 0$ using ANOVA for multiple regression. The wavelength of the spiking wave was determined by first estimating $\mathbf{k}$ in eq. 19 by least squares and then using eq. 12.

Spiking wave analysis of pyramidal neurons

Is the activity of CA1 pyramidal neurons organized as a traveling wave during theta oscillations? To address this questions the population mean phase at each grid location $\mu(\mathbf{x})$ (eq. 17) was computed from the mean phases μ_k of significantly phase-locked active pyramidal units only, and the spiking wave hypothesis was tested as above (eq. 19, Fig. S14a).

Alternatively, significantly phase-locked active pyramidal neurons were split into two groups based on their anatomical location with respect to the wave propagation direction inferred from the multiunit analysis. Under the spiking wave hypothesis the preferred phases of the pyramidal cells in the two groups should be different, while under the null hypothesis they should be the same. A two sample test of mean angles was therefore carried out to statistically distinguish between the two alternatives [6] (Fig. S14b).

Recorded single units were classified as active pyramidal cells if they met all of the following criteria [7, 8, 9]: (1) mean firing rate below 10 Hz; (2) mean spike width above 0.3 ms; (3) presence of clear place field with peak rate above 3 Hz; (Fig. S7, S8, S9, S10, S11). Only spikes fired when the rat was running (speed above 10 cm/s) were used in computing place fields, phase value distributions, and mean phases of active pyramidal cells (Fig. S10, S11, S12) in order to exclude activity associated with ripple bursts and other non-theta states (occurring when the rat was drinking water or grooming at the ends of the track).

2 Movies

Filename	Description
wave_6x5	Traveling theta wave in rat 1 implanted with 6x5 grid.
wave_4x8	Traveling theta wave in rat 2 implanted with 4x8 grid.
wave_5x6	Traveling theta wave in rat 3 implanted with 5x6 grid.

Each movie frame consists of M by N squares corresponding to the recording grid size. The color of the square on the m^{th} row and n^{th} column shows $u(\mathbf{x_{ij}}, t)/\rho(\mathbf{x_{ij}}, t) = \mathrm{Re}(e^{j\varphi(\mathbf{x_{ij}},t)}) = \cos(\varphi(\mathbf{x_{ij}}, t))$, i.e. the amplitude normalized theta trace recorded at location $\mathbf{x_{ij}}$. If no signal was recorded at a given grid location the square is black. Notice that no spatial filtering of any kind was performed. Successive frames show successive time points and time in the movies is slowed down by a factor of ~ 14, i.e. 1 second in the movies corresponds to 72 milliseconds of real time, and therefore to approximately half a theta cycle.

References

[1] Paxinos G. and Watson C. *The Rat Brain in Stereotaxic Coordinates*. Academic Press, 4th edition, 1998.

[2] Swanson L.W. *Brain Maps: Structure of the Rat Brain*. Elsevier, 2nd edition, 1998.

[3] Tyszka J.M., Readhead C., Bearer E.L., Pautler R.G., and Jacobs R.E. Statistical diffusion tensor histology reveals regional dysmyelination effects in the shiverer mouse mutant. *Neuroimage*, 29(4):1058–1065, 2006.

[4] Buzsáki G., Leung L.W.S., and Vanderwolf C.H. Cellular bases of hippocampal EEG in the behaving rat. *Brain Res. Rev.*, 6:139–171, 1983.

[5] Siapas A.G., Lubenov E.V., and Wilson M.A. Prefrontal phase-locking to hippocampal theta oscillations. *Neuron*, 46:141–151, 2005.

[6] Zar J.H. *Biostatistical Analysis*. Prentice Hall, 4th edition, 1999.

[7] Ranck J.B. Jr. Studies on single neurons in dorsal hippocampal formation and septum in unrestrained rats. I. Behavioral correlates and firing repertoires. *Exp. Neurol.*, 41(2):461–531, 1973.

[8] Fox S.E. and Ranck J.B. Electrophysiological characteristics of hippocampal complex-spike cells and theta cells. *Exp. Brain Res.*, 41:399–410, 1981.

[9] Csicsvari J., Hirase H., Czurko A., Mamiya A., and Buzsaki G. Oscillatory coupling of hippocampal pyramidal cells and interneurons in the behaving rat. *J. Neurosci.*, 19(1):274–287, 1999.

[10] Petrovich G.D., Canteras N.S., and Swanson L.W. Combinatorial amygdalar inputs to hippocampal domains and hypothalamic behavior systems. *Brain Res. Rev.*, 38(1-2):247–289, 2001.

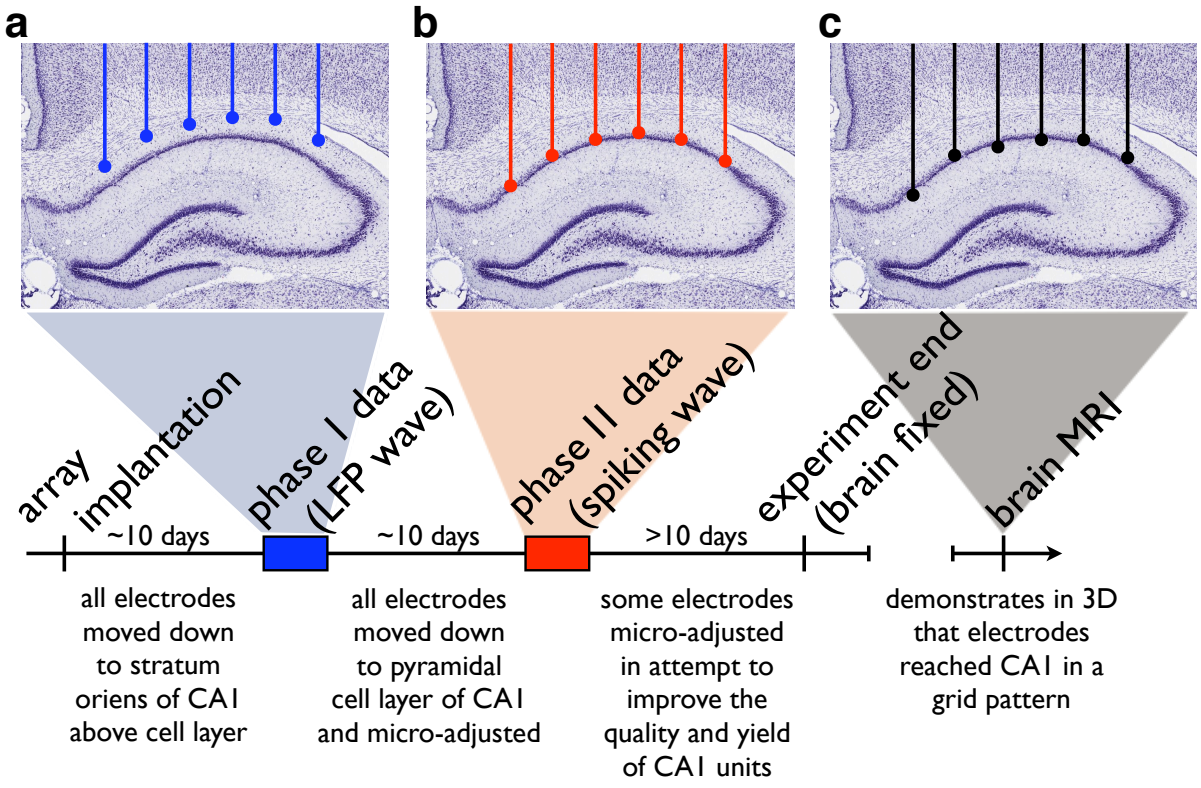

FIGURE S 1: **Experimental timeline.** Timeline shows **(a)** phase 1 (blue rectangle) and **(b)** phase 2 (red rectangle) data acquisition periods relative to intervening periods of electrode adjustments. Coronal sections on top illustrate corresponding target electrode depths (not actual data). Notice that all electrodes are moved down between phase 1 and phase 2, and that some electrodes are further micro-adjusted after phase 2. Both MRI and histological analysis reflect only the final electrode depths at the end of the experiment **(c)**.

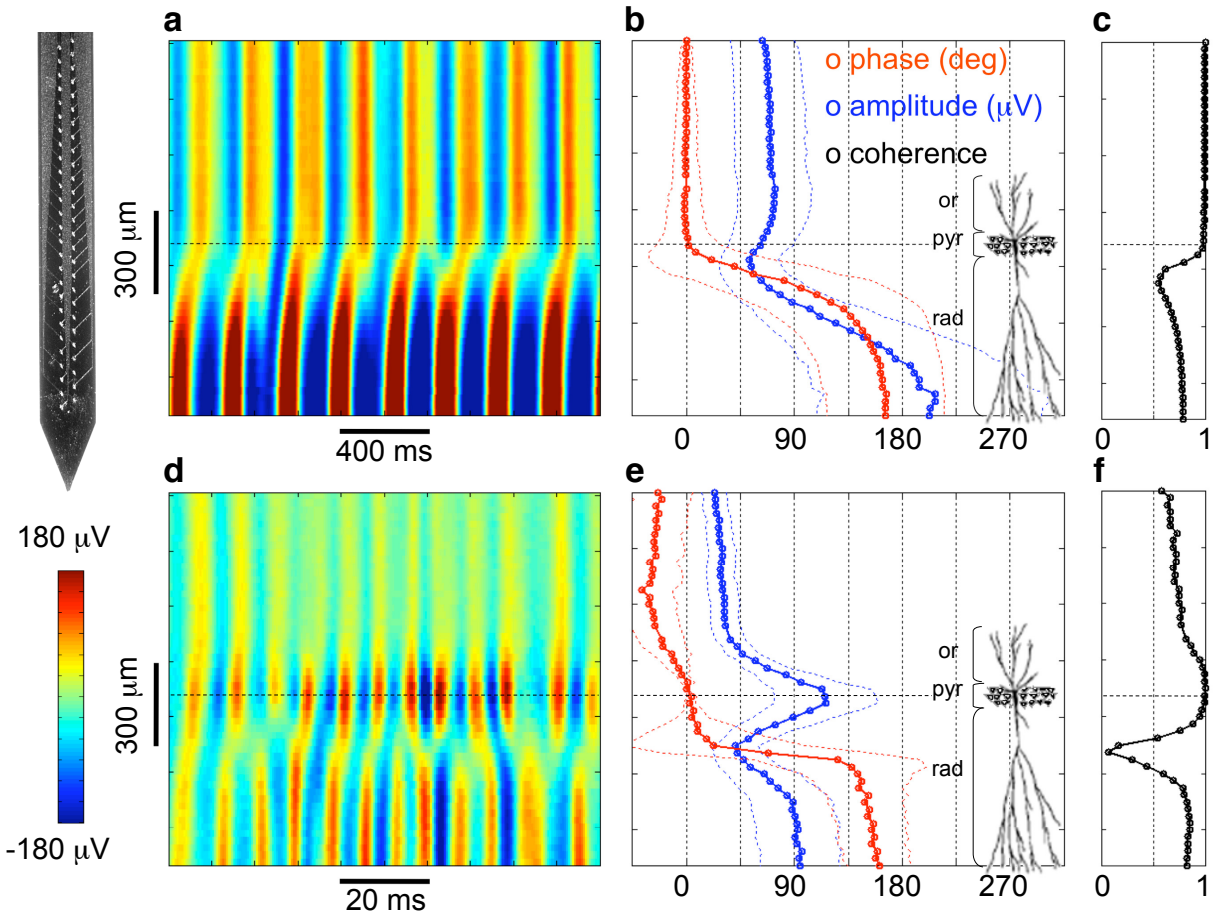

FIGURE S 2: **Interlaminar depth profile of theta oscillations and ripples under urethane anesthesia.** Data were simultaneously recorded above, at, and below the CA1 pyramidal cell layer (pyr) in a urethane anesthetized rat using a 54-site silicon probe (1.325 mm vertical span, two staggered columns 43 μm apart, 25 μm vertical site spacing across columns). In all panels data from both columns are combined and ordered from most superficial (top) to deepest (bottom). **(a)** Pseudocolor plot of LFPs filtered between 4 and 10 Hz during a period with prominent theta oscillations. Notice the vertical stripes above the horizontal line, indicating that theta oscillations are in phase throughout a vertical extent of at least 600 μm. **(b)** Theta amplitudes (blue) and phase deviations (red) with respect to the most superficially recorded signal. Solid and interrupted lines show means and standard deviations, respectively. Mean theta phase deviations are within 2 degrees throughout a 600 μm vertical extent including stratum oriens (or). Theta starts shifting phase abruptly near the border of stratum radiatum (rad) with an initial depth gradient of $\approx 0.6^{\circ}/\mu m$. **(c)** Theta coherence with respect to the same reference signal as in (b). **(d)** Pseudocolor plot of LFPs filtered between 80 and 250 Hz during a ripple. **(e)** Ripple amplitude (blue) and phase deviations (red) with respect to the signal with maximal ripple amplitude. The depth marked by highest ripple amplitude corresponds to the abrupt start of theta phase shift. **(f)** Ripple coherence with respect to same reference as in (e).

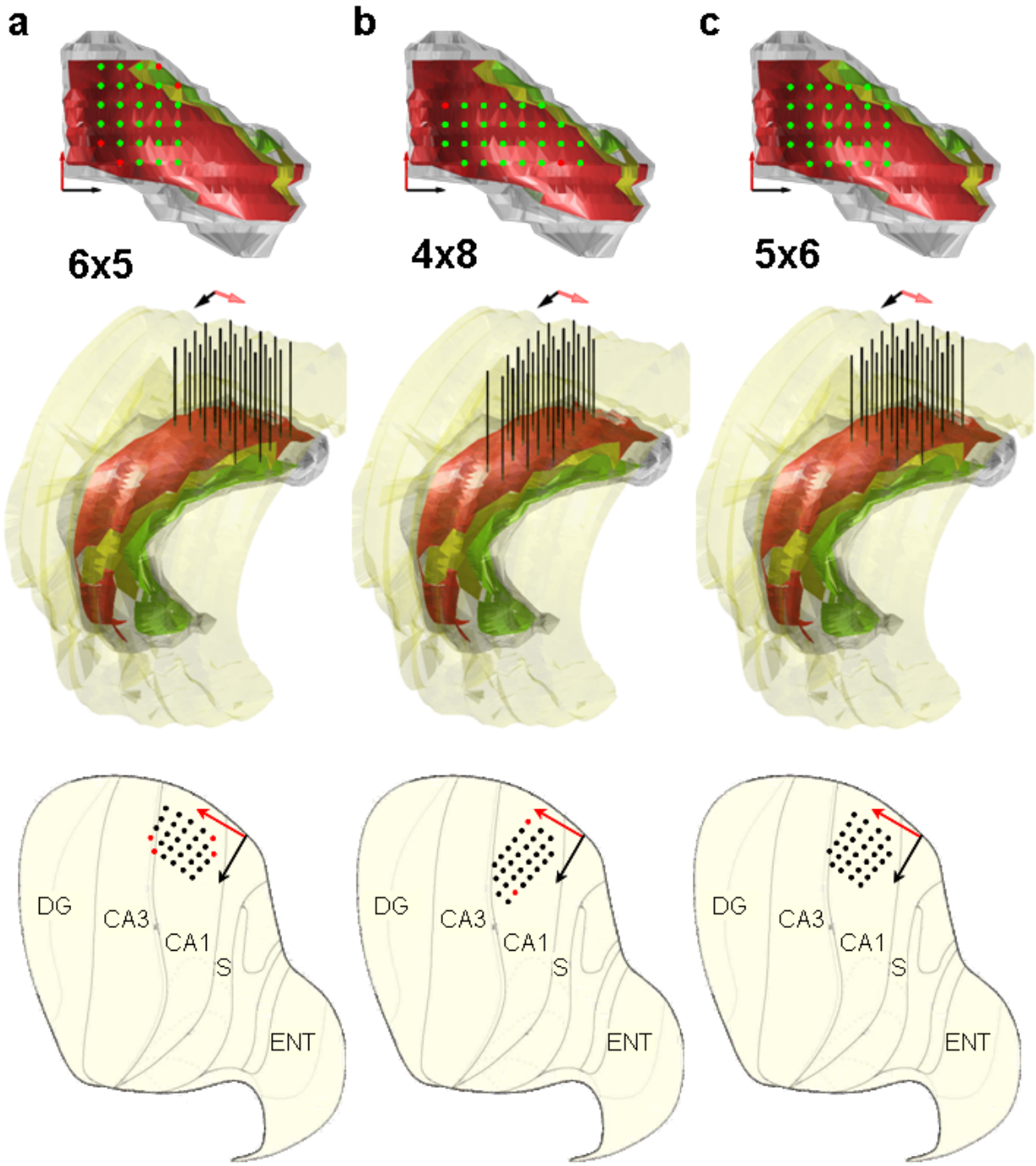

FIGURE S 3: **Microdrive grid configurations. (a-c) middle** 3D model of the right hippocampus (gray) with the pyramidal cell layer of CA1 (red), CA2 (yellow), CA3 (green), and cortex (transparent yellow). Black rods show the configuration of tetrodes lowered to CA1 for the (a) 6x5, (b) 4x8, and (c) 5x6 grid. Red and black arrows are 1 mm long and point in the rostral and lateral anatomical directions, respectively. **top** Rotated top-down view with cortex removed and tetrodes marked by color dots. Data were successfully obtained from locations marked by green dots. **bottom** Flatmap of the unfolded hippocampal formation with dots marking tetrode targets in CA1 [2]. The location of tetrode targets (dots) was estimated using flatmap projections of coronal sections (Fig. 6 in [10]). In the target region the mediolateral axis (black arrow) forms and angle of about 30° with respect to the septotemporal axis (border between CA1 and CA3).

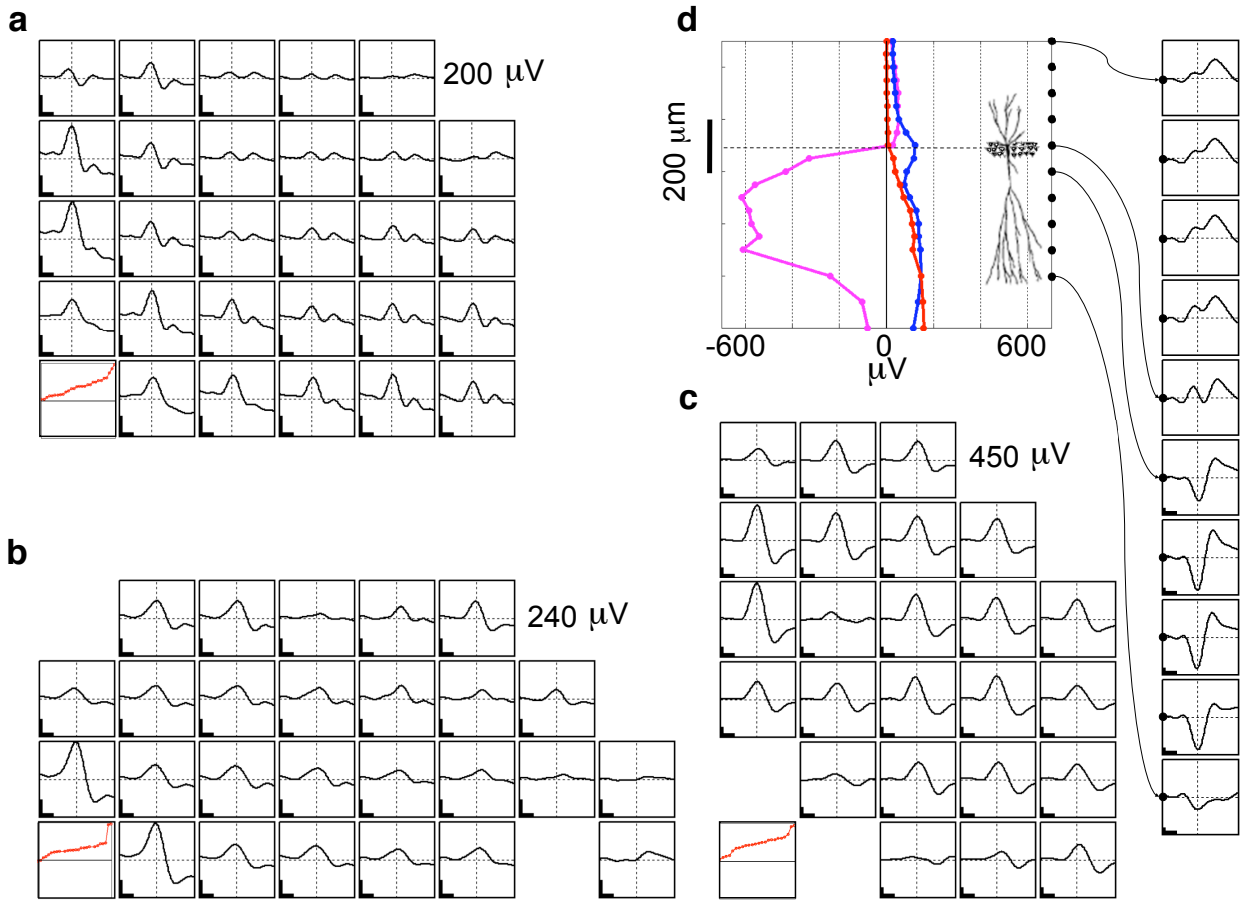

FIGURE S 4: **Sharp-wave analysis (a-c)** Small panels show the average sharp-wave (SPW) recorded at each grid point of the (a) 5x6, (b) 4x8, and (c) 6x5 grids when tetrodes were targeting stratum oriens of CA1 in phase 1. All panels are 300 ms in duration and the horizontal and vertical lines mark 0 μV and the peak of the SPW, respectively. The calibration bars are 50 ms and 100 μV everywhere. The maximal SPW amplitude across the electrodes of each grid is printed in the upper right corner. The red points in the bottom left panels show the sorted SPW amplitudes across the electrodes of each grid. Notice that the SPW amplitudes are positive at all grid locations. **(d)** Small panels show the average SPW chronically recorded at different depths with respect to the CA1 pyramidal cell layer using a silicon probe with 50 μm vertical site spacing. The large panel shows SPW amplitude (magenta), ripple amplitude (blue), and phase of theta oscillations (red) as a function of depth (y-axis). The red and blue curves are replotted from Fig. 1b and Fig. 1e, respectively. Notice that ripple amplitude peaks, SPW polarity reverses, and theta oscillations abruptly start shifting in phase at the exact same depth, corresponding to the pyramidal cell layer. The fact that SPWs have positive polarity at all grid points (a-c) therefore demonstrates that all grid electrodes were indeed positioned above the CA1 pyramidal cell layer as intended.

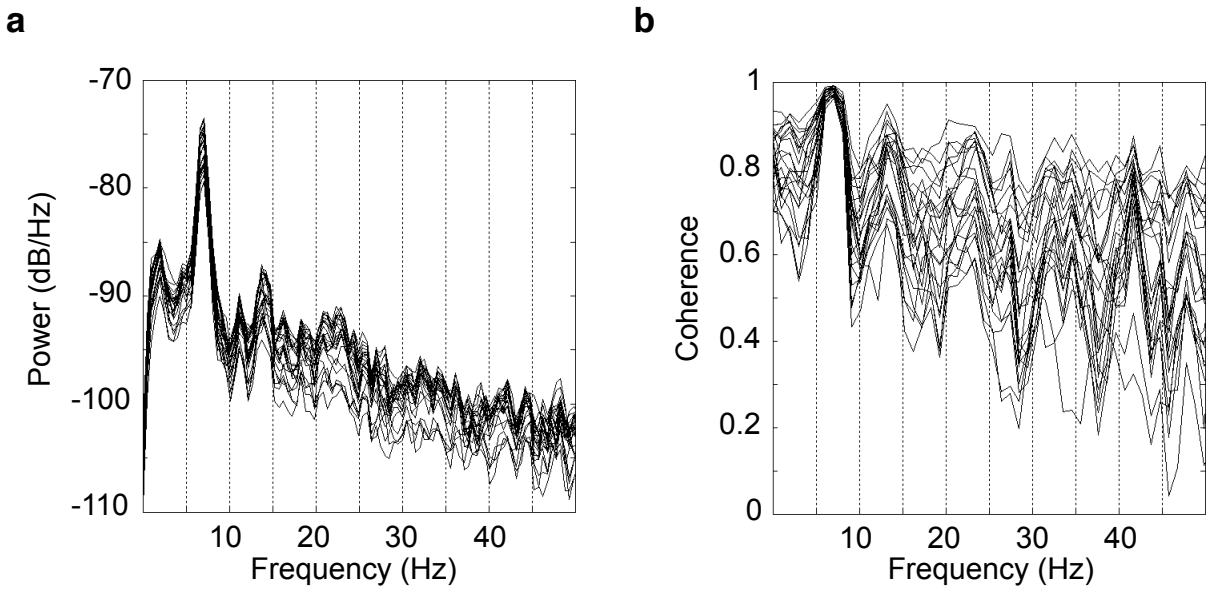

FIGURE S 5: **Power spectra and coherence of LFPs (a)** Power spectral density estimates of 24 simultaneously recorded LFPs from the 6x5 grid. The analysis is based on a 15 sec period with pronounced theta oscillations. Notice that the spectral estimates of all 24 LFPs have a peak at the same frequency of 7 Hz. **(b)** Corresponding coherence estimates between a reference LFP recorded from the grid center and the remaining LFPs. Notice the almost perfect (≈ 1) coherence values at 7 Hz demonstrating that theta oscillations are coherent across the recording array.

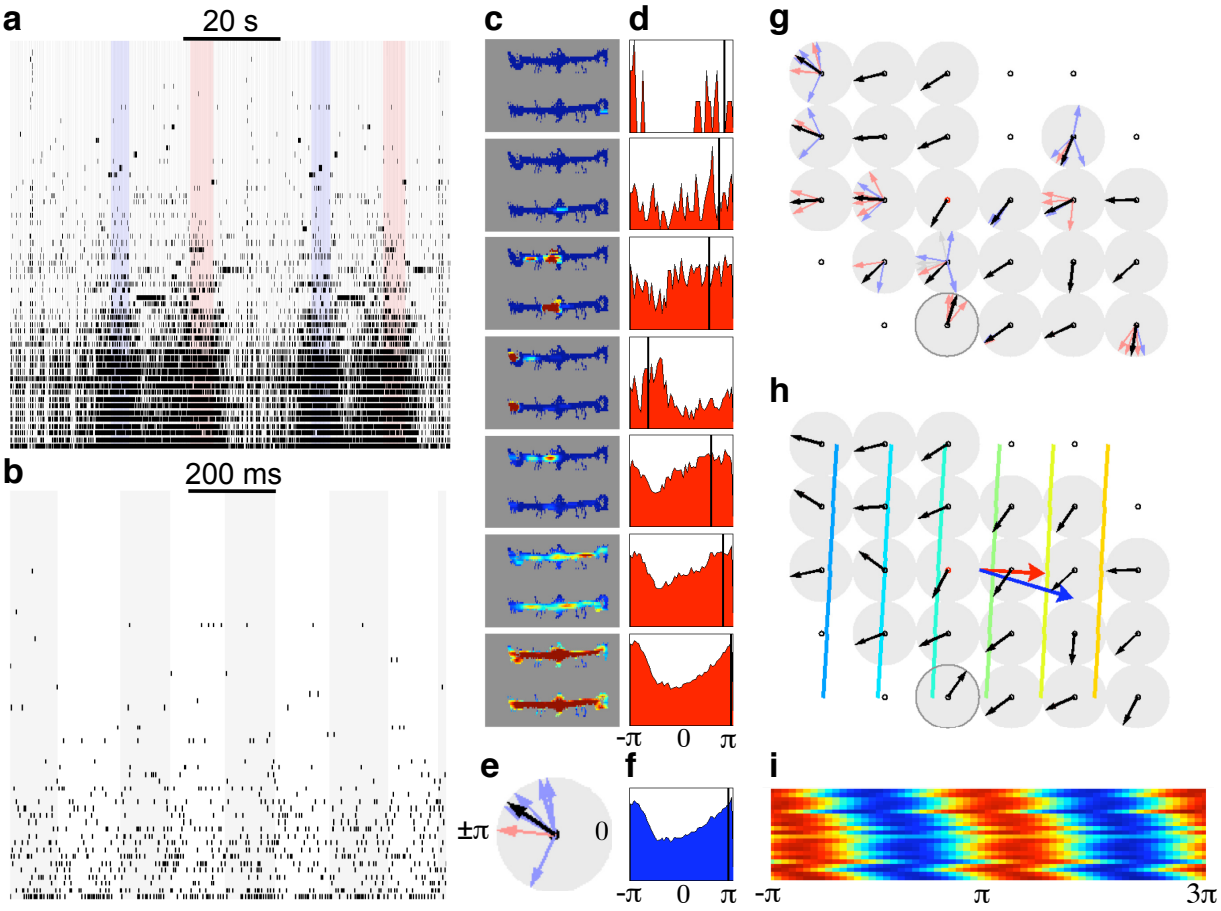

FIGURE S 6: **Topographic profile of spiking theta phase preference. (a)** Rasters of unit activity during two round trip laps on a linear track. Sixty units are ordered by mean firing rate and colored stripes mark periods of running in opposite directions. Notice the repeating pattern of firing across the two laps due to the place specificity of pyramidal neurons. **(b)** Detailed view of 1 sec of the rasters in (a). The alternating stripes mark consecutive theta cycle. Notice the sparsity of firing within individual cycles. **(c)** Directional firing rate maps for units recorded on one tetrode. **(d)** Theta phase distributions corresponding to the units in (c). Black vertical lines mark the preferred phase of each unit. **(e)** Circular display of the preferred phases of the units in (d). Blue and red arrows indicate putative pyramidal cells and interneurons, respectively. Black arrow is the population mean phase. **(f)** Theta phase distribution corresponding to the multiunit formed by combining all spikes from all units recorded on the tetrode. The preferred phase of the multiunit closely matches the population mean phase. **(g)** Preferred phases for all units were computed with respect to a single LFP trace (red circle) and displayed as in (e). For some tetrodes the spiking activity could not be reliably sorted into single units and the preferred phase of the multiunit is displayed as the black arrow. **(h)** Arrows mark the preferred phases of the multiunits recorded at each location on the grid. Notice the clockwise rotation of the arrows from the medial to the lateral columns with the exception of the marked outlier. Colored lines are the level curves of the best linear fit to the unfolded preferred phases. Red and blue arrows mark the direction of wave propagation inferred from spiking activity and LFPs, respectively. The length of the arrows is 1/24 of the inferred spatial wavelength. **(i)** Pseudocolor plot of normalized multiunit theta phase distributions displayed over two cycles. Each row corresponds to a location on the grid and rows are ordered from medial (top) to lateral (bottom). The slanted appearance indicates that the spiking probability is modulated in a wave pattern.

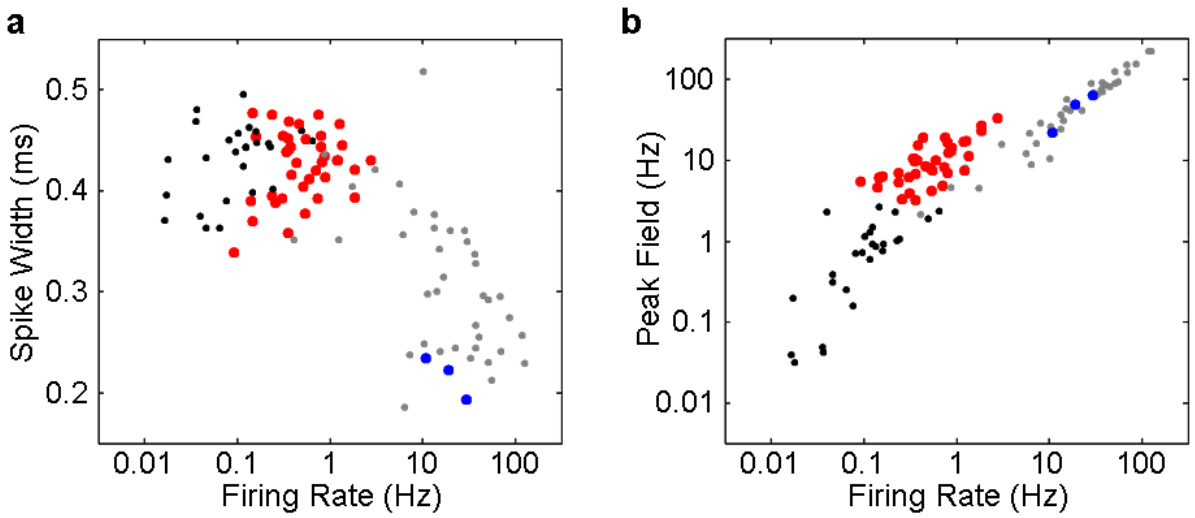

FIGURE S 7: **Unit classification. (a)** Firing rate (Hz) vs. spike width (ms) for all simultaneously recorded units in the 4x8 array. Spike width was measured in waveforms filtered between 0.6 and 6 KHz. Units are color coded as follows: 38 active pyramidal cells with clear place fields on the track (red), 3 interneurons (blue), 38 multiunits (gray), and 26 low firing units–likely pyramidal cells without place fields on the track (black). Pyramidal cells have firing rates < 10 Hz (mean of 0.67 Hz and 0.14 Hz for active and low firing cells, respectively) and spike widths > 0.3 ms (mean of 0.43 ms). Multiunits exhibit high rates and intermediate widths, as they are likely composed of spikes generated by both pyramidal cells and interneurons in various proportions. **(b)** Firing rate (Hz) vs. peak place field rate (Hz). Active pyramidal cells (red) have peak place field rates > 3 Hz (mean of 10.77 Hz and 0.94 Hz for active and low firing cells, respectively). The pyramidal unit wave analysis (Fig. S14) is based on the firing of the active pyramidal cells (red).

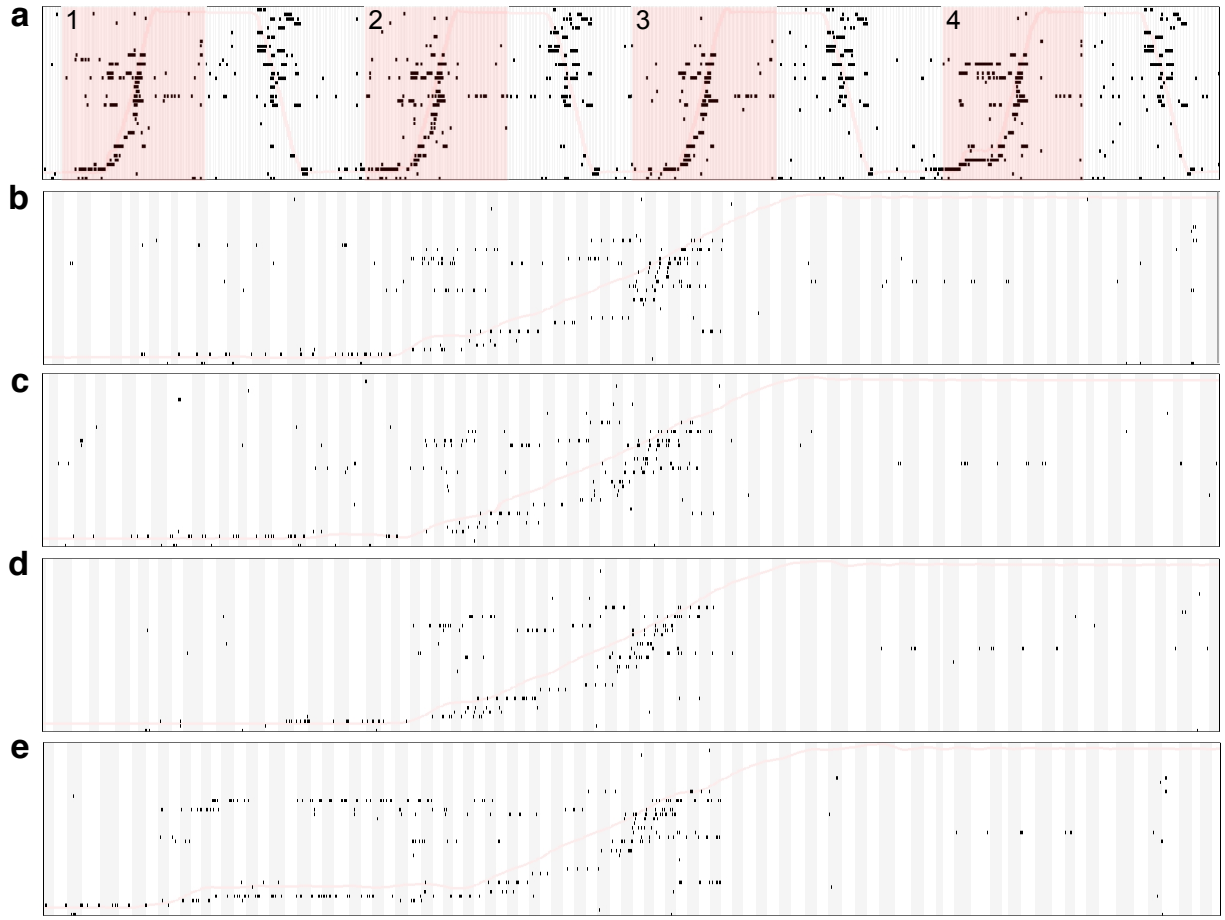

FIGURE S 8: **Rasters of left-to-right track traversals. (a)** Rasters of the 38 active pyramidal units participating in the unit wave analysis during four round trip laps on the linear track (100 sec). Units are ordered by the location of their directional left-to-right place field centers and all spikes are shown. Units with place fields at the left end of the track are shown on the bottom and units with place fields at the right end are shown on the top. Pale red line marks the position of the rat along the track. **(b-e)** Expanded views ($\sim$ 8 sec) of the four left-to-right laps highlighted in (a). The alternating stripes mark consecutive theta cycle. Notice the repeating pattern of firing across the four laps due to the place specificity of pyramidal neurons.

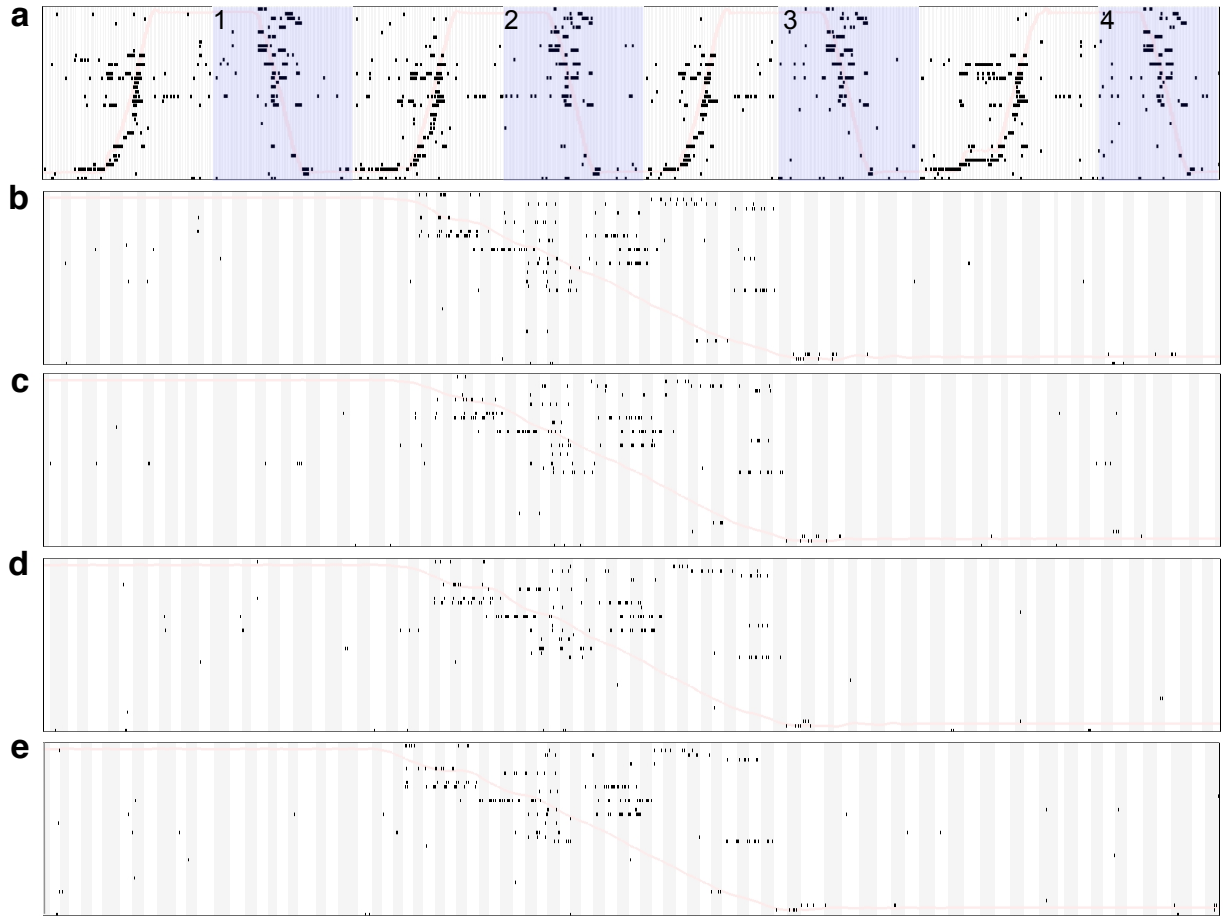

FIGURE S 9: **Rasters of right-to-left track traversals. (a)** Same as Fig. S8a, but with right-to-left laps highlighted. **(b-e)** Expanded views ($\sim$ 8 sec) of the four right-to-left laps highlighted in (a).

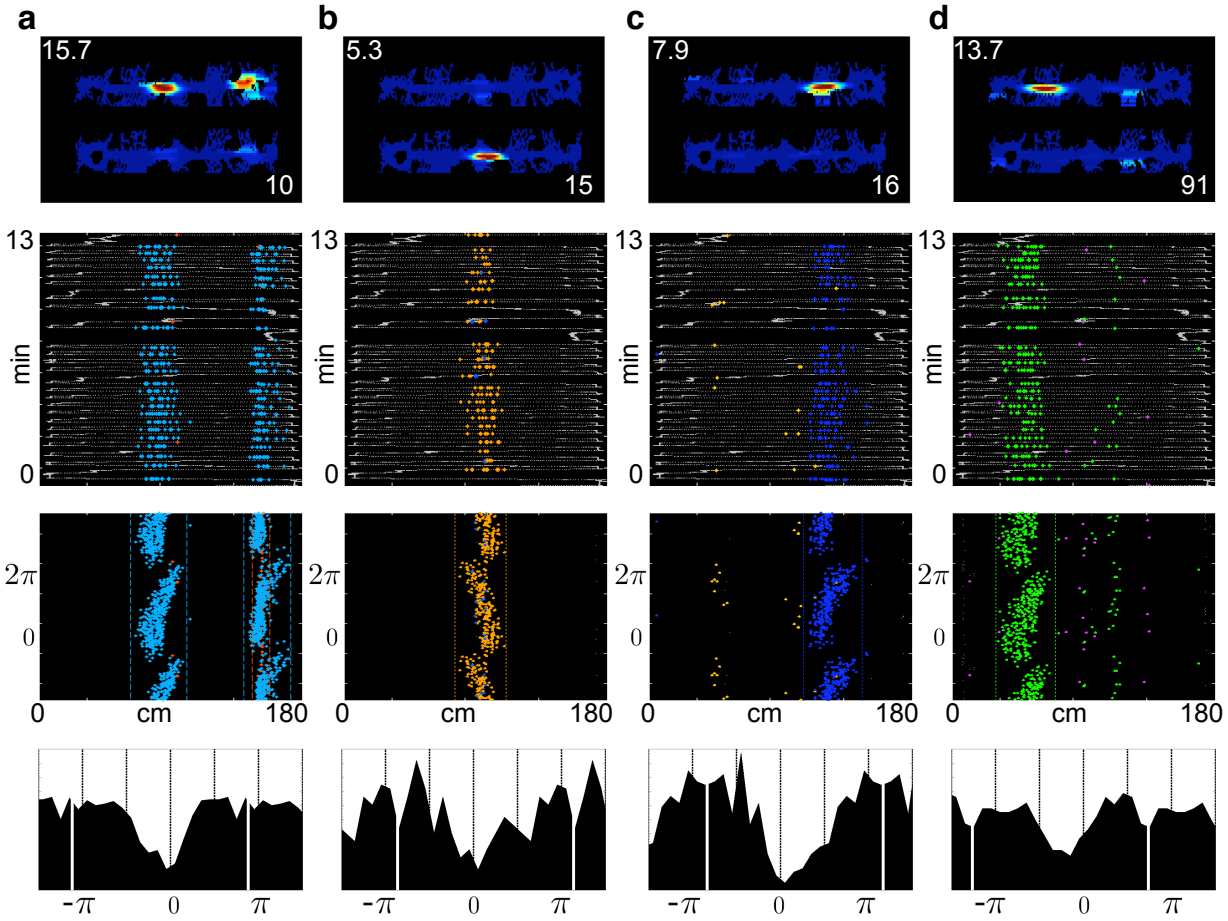

FIGURE S 10: **Examples of active pyramidal cells. (a-d)** Four active pyramidal cells recorded on three different tetrodes of the 4x8 array. The panels in each column show data for one pyramidal cell. From top to bottom: (1) directional place field maps with left-to-right direction on the bottom and right-to-left on top; peak firing rate in Hz is shown in the top left corner and the cell id number in the bottom right; (2) gray line shows the position of the rat over time and the color dots mark the position and time of spikes; (3) dots mark position and phase of spikes with respect to the theta cycle; (4) theta phase value distribution of spikes; the distribution is replotted for a quarter cycle on each side and the white lines mark the mean phase of the cell.

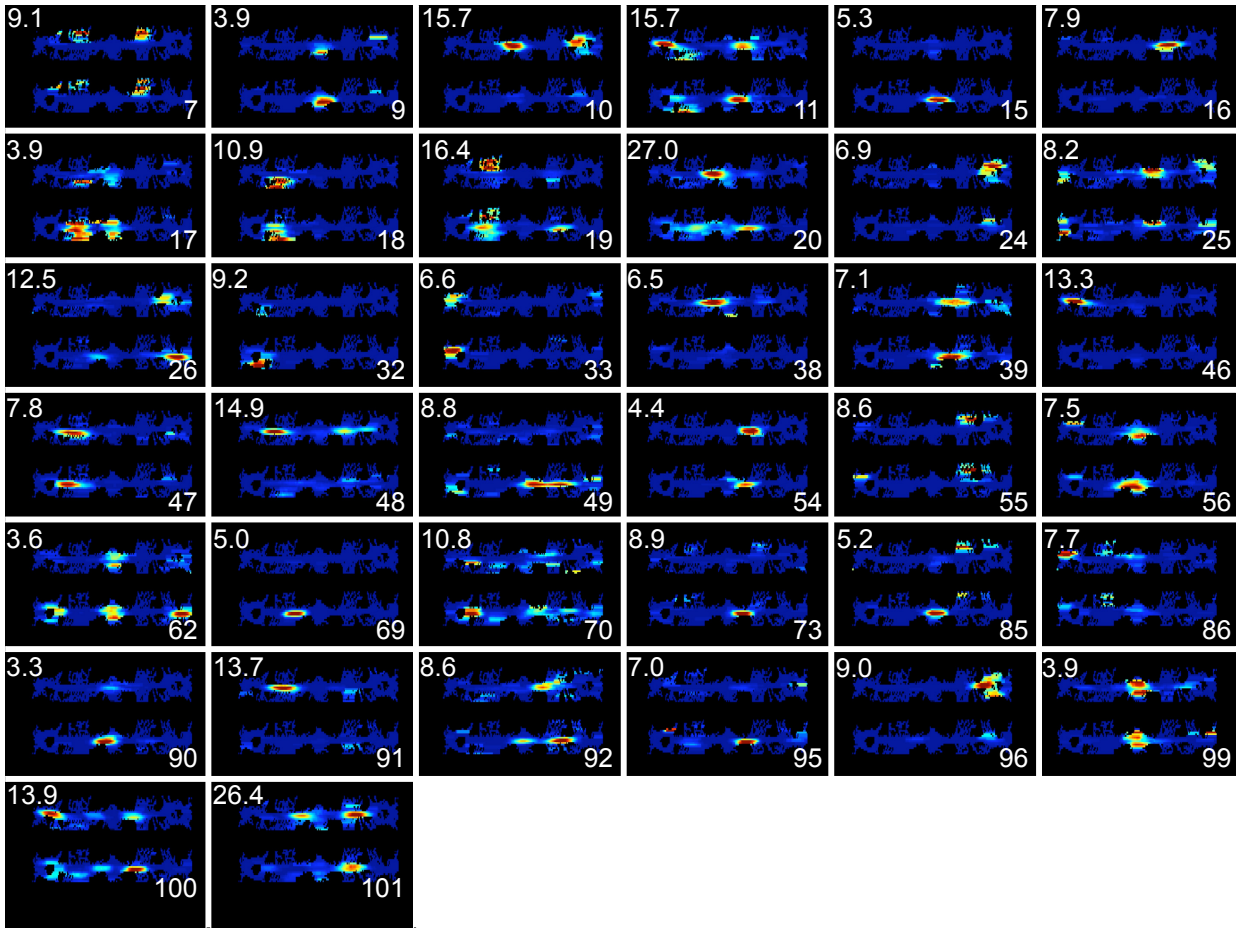

FIGURE S 11: **Place fields of active pyramidal cells.** Panels show directional place field maps for all 38 simultaneously recorded (4x8 array) pyramidal cells active on the track. Within each panel the right-to-left map is shown on top and the left-to-right map on the bottom. The colormap of each panel is adjusted to the peak firing rate for the cell, displayed (in Hz) in the top left corner. The cell id is displayed in the bottom right corner.

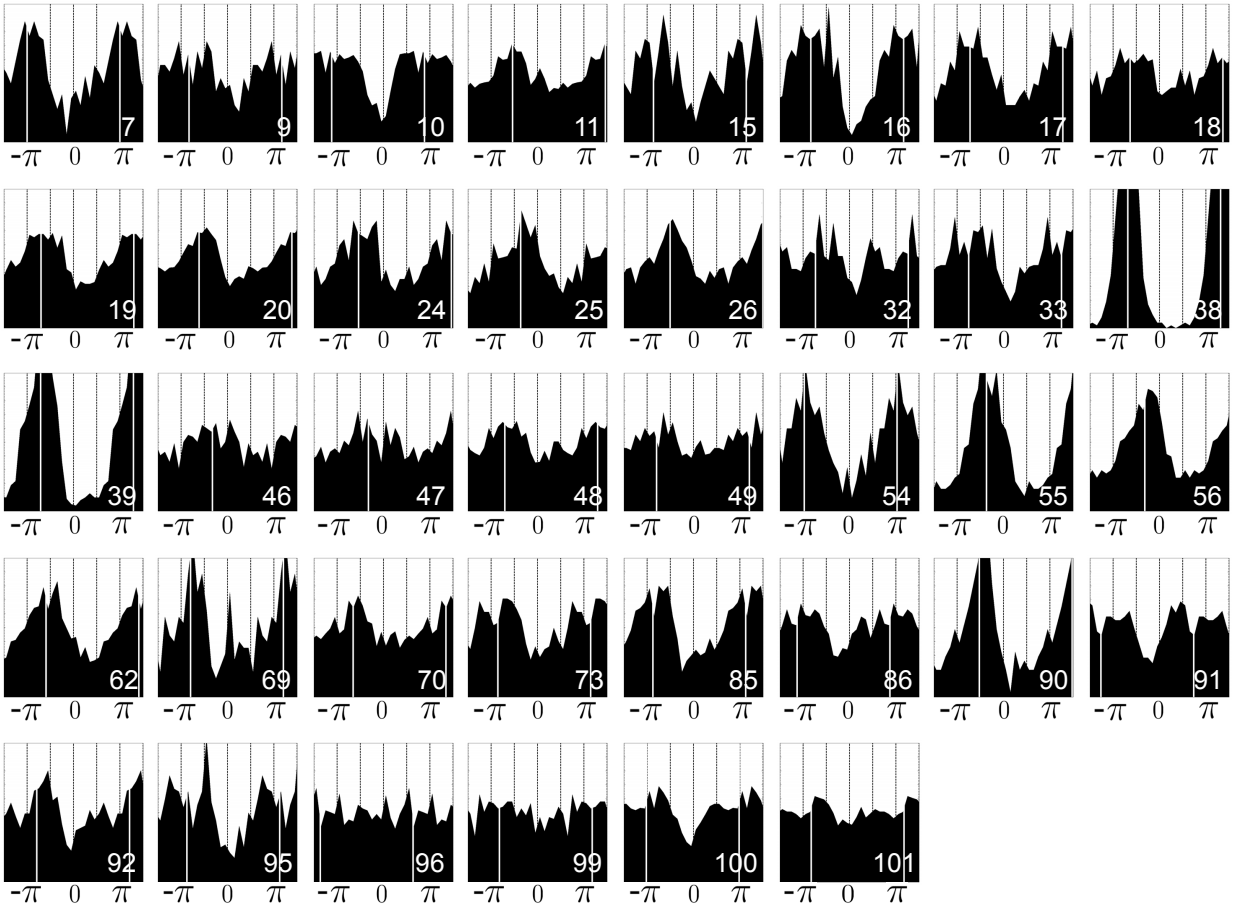

FIGURE S 12: **Phase value distributions of active pyramidal cells.** Panels show theta phase value distributions corresponding to each of the 38 simultaneously recorded (4x8 array) pyramidal cells active on the track. The distributions are computed with respect to a single reference LFP theta trace and are replotted for a quarter cycle on each side. The white vertical lines mark the mean phase for each cell (shown as arrows in Fig. S14a). The cell id is displayed in the bottom right corner. Raw histogram counts are normalized by the total count for each cell and vertical scales are the same across all panels. All but 3 cells (id: 32, 96, 99) were significantly phase-locked ($p < 0.01$, Rayleigh test) and used in the pyramidal cell wave analysis. Notice that panels are not arranged in correspondence to cell location in the recording grid, since the number of active cells on each tetrode was different.

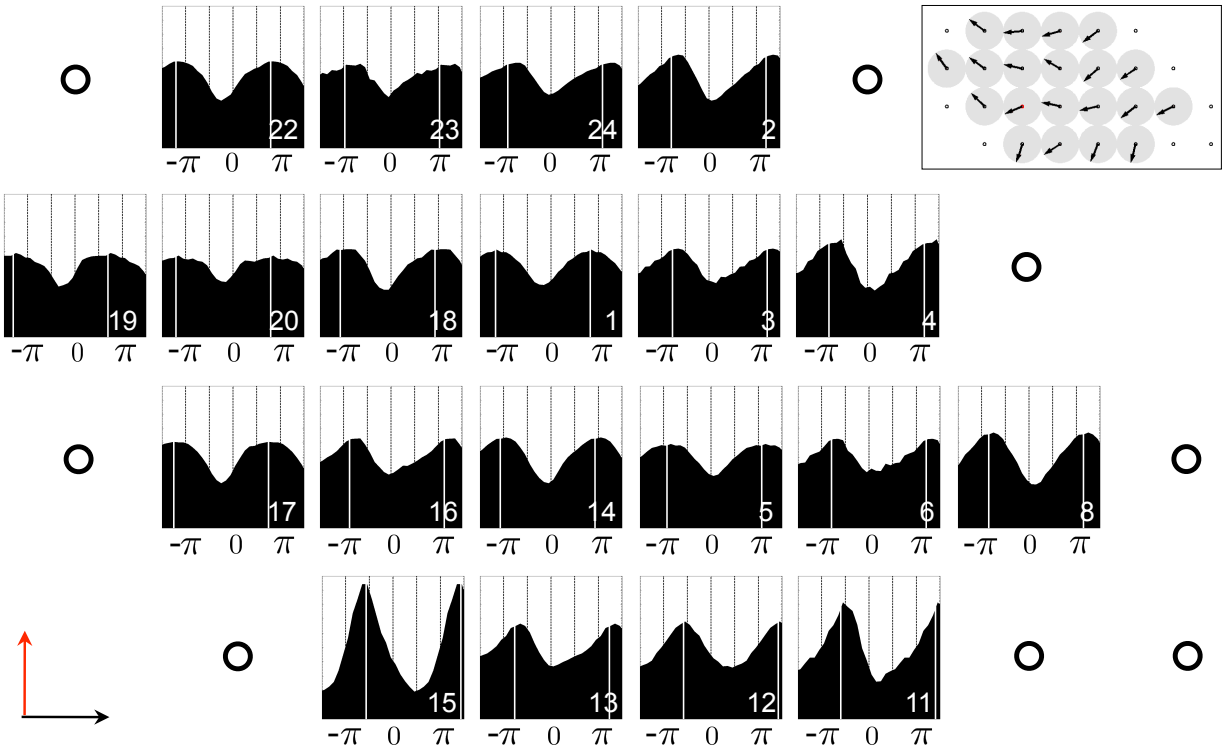

FIGURE S 13: **Phase value distributions of tetrode multiunits.** Panels show theta phase value distributions corresponding to all spikes recorded on each tetrode of the 4x8 array. The distributions are computed with respect to a single reference LFP theta trace and are replotted for a quarter cycle on each side. The white vertical lines mark the mean phase for each tetrode multiunit. The tetrode id is displayed in the bottom right corner. Raw histogram counts are normalized by the total count for each multiunit and vertical scales are the same across all panels. Panels are arranged according to the location of the source tetrode in the array. The perpendicular arrows in the bottom left corner point rostrally (red) and laterally (black). The inset displays the mean phase for each tetrode multiunit as an arrow (same as Fig. 5b).

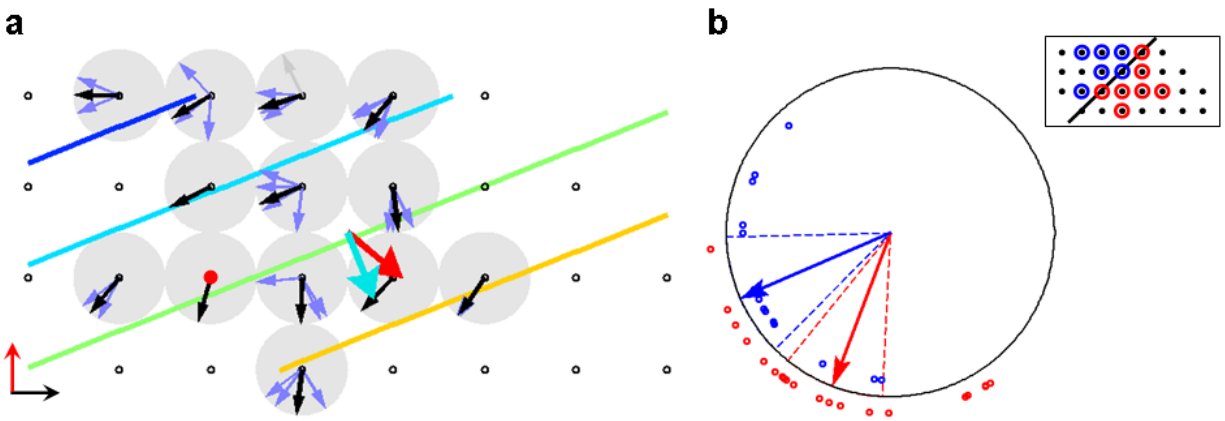

FIGURE S 14: **Topographic profile of pyramidal cell theta phase preference. (a)** Black arrows show the population mean phase of active pyramidal cells at each grid location with respect to a single reference theta trace (red dot) in the 4x8 array (N=38 active pyramidal units). Blue arrows show the mean phases of individual pyramidal cells that are phase-locked ($p < 0.01$) and gray arrows–the mean phases of pyramidal cells that are not phase-locked. Colored lines are the level curves of the best linear fit to the unfolded preferred phases of the phase-locked units. The red and cyan arrows in the center mark the direction of wave propagation θ of multiunit spiking activity and pyramidal unit activity, respectively. The arrow lengths are proportional to the corresponding spatial wavelengths λ of the multiunit and pyramidal unit waves. The actual values are as follows–multiunit wave: $\theta = -40\ ^\circ$, $\lambda = 9.3$ mm, ANOVA $p < 0.0006$, $R^2 = 0.59$; pyramidal unit wave: $\theta = -68\ ^\circ$, $\lambda = 9.4$ mm, ANOVA $p < 0.03$, $R^2 = 0.51$; The perpendicular arrows in the bottom left corner point rostrally (red) and laterally (black). **(b)** The 38 simultaneously recorded pyramidal cells were divided in two groups (red and blue) based on the anatomical location of the source tetrode (inset). The red and blue dots at the edge of the black circle show the mean phases of individual phase-locked pyramidal cells, arrows show the population mean phases of the red and blue groups, and interrupted lines mark the 0.95% confidence intervals of the two population means. The means of the red and blue groups are clearly different ($p < 0.001$, two-sample test of mean angles) therefore rejecting the null hypothesis that pyramidal cell activity is synchronous across the array in favor of the wave propagation alternative. Notice that the array was divided in two by a 45 degree line (black line in inset) approximately parallel to the wavefront of multiunit activity and offset in order to equalize the size of the two groups of pyramidal cells.

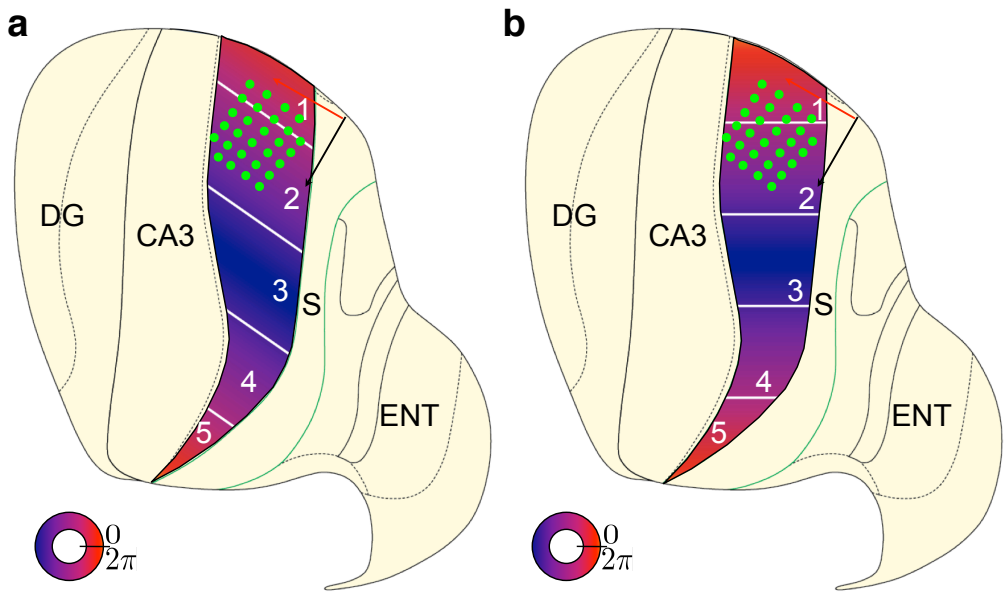

FIGURE S 15: **Flatmap view of theta phase across CA1. (a)** Flatmap view of the hippocampal formation. The color gradient shows the instantaneous phase of theta oscillations (circular inset) extrapolated throughout CA1 in the case of mediolateral propagation direction (30° with respect to the septotemporal axis as determined by the border between CA1 and CA3). The green dots show a reference grid (5x6) where actual measurements were made. The white lines (wavefronts) divide CA1 into 5 numbered bands, such that the phase of theta oscillations is approximately the same within each (same color). The numbered bands correspond to the 5 septotemporal levels (rows) considered in Fig. S16h,i and Fig. S17. Notice that despite the presence of a transverse component in the wave propagation direction (which tilts the wavefronts) CA1 can be conceived as a collection of (tilted) equiphase bands, orderly stacked along the septotemporal axis. This view is at the core of the interpretation we consider in the text (Fig. 6). It is appropriate as long as the tilt is not excessive, i.e. as long as the transverse component of the propagation direction is not much larger than the septotemporal one. Experimentally, the septotemporal component is larger and therefore this condition is met. **(b)** Same as (a) in the case of a purely septotemporal wave propagation direction, i.e. without a transverse component. Notice that in this case the 5 equiphase sections have different shapes, but the view of CA1 as a stack of equiphase bands still holds. Therefore, the presence of a transverse component in the wave propagation direction does not affect the interpretation we consider, granted its magnitude does not much exceed that of the septotemporal component.

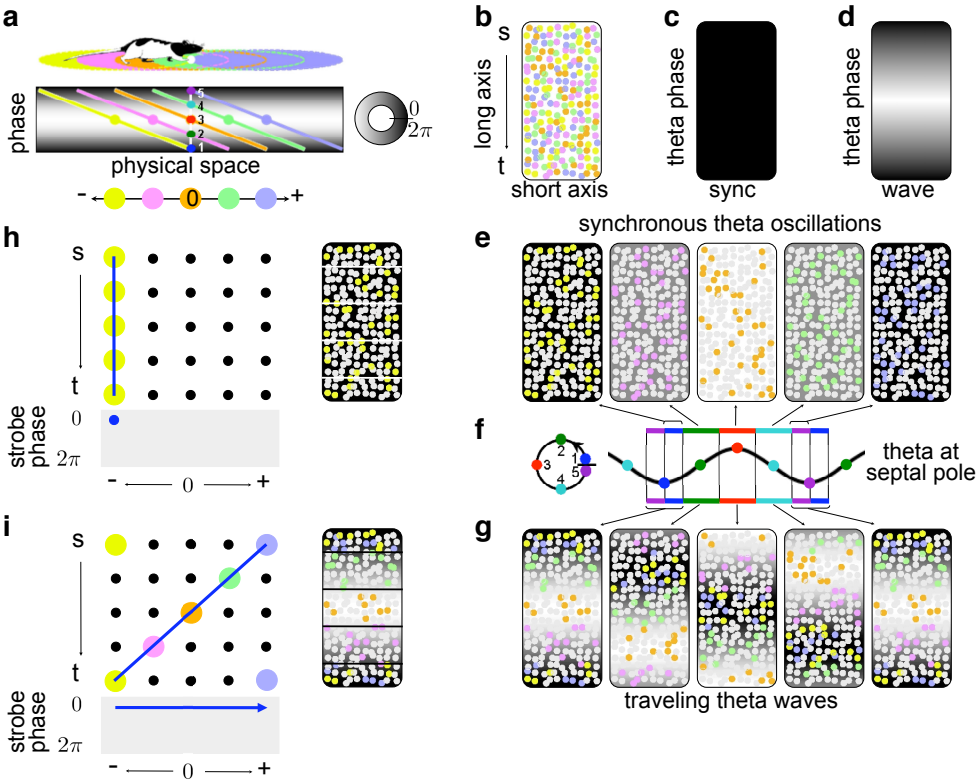

FIGURE S 16: **Construction of the hippocampal representation of physical space. (a)** Ellipses show CA1 place fields overlapping the position of the rat's head in a linear environment. Place fields are assumed to be roughly the same size throughout CA1. The slanted lines below are idealized phase precession relations for the cells above. The horizontal axis is physical location and the vertical axis is the local phase of theta oscillations, indicated by the gray scale value of the background. The white line shows the rat's position and the numbered color dots mark 5 strobe phases within the theta cycle. **(b)** Unfolded map of CA1 with dots showing all place cells with fields overlapping the rat's position. The colors of the cells represent their place field centers. **(c-d)** The grayscale value indicates the instantaneous phase of theta throughout CA1 in the case of synchronized theta oscillations (c) and traveling theta waves (d). **(e)** Patterns of CA1 activity if theta oscillations are synchronized. Each panel is as in (b), but only the subset of cells active within a narrow time window is colored. The background shows the phase of local theta. Panels from left to right correspond to the 5 strobe phases in (a), also illustrated in (f) below. Because of synchrony at each time point a single phase of theta is mapped across the hippocampus (c) and therefore only cells with precession curves intersecting the white line in (a) fire. **(f)** A theta cycle from the septal pole is displayed to illustrate the strobe phases and time windows at which the activity in (e) and (g) are illustrated. **(g)** Patterns of CA1 activity if theta oscillations are traveling waves. At each time point a range of local theta phases is mapped across the hippocampus in accordance with the spatial wavelength and propagation direction (d). The rat's position and the local phase of theta determine which place cells are active at each anatomical position in accordance with (a). **(h)** Collapsed representation of the activity pattern in the first panel of (e) (Fig. S17a maps all panels). The septotemporal axis is divided into 5 bands and within each band 5 field center locations are considered, giving the matrix of black dots. The transverse axis is collapsed and the field centers of the cells active within each band is highlighted. The field centers of the co-active cells are then connected–the color of the line indicates the strobe phase. Projecting the line to the physical space axis shows that the instantaneous CA1 output represents a point of physical space. **(i)** Collapsed representation for the first panel in (g) (Fig. S17b maps all panels). The construction is identical to (h). In this case, the line connecting the field centers of co-active cells is slanted and its projection shows that CA1 activity represents a segment of physical space.

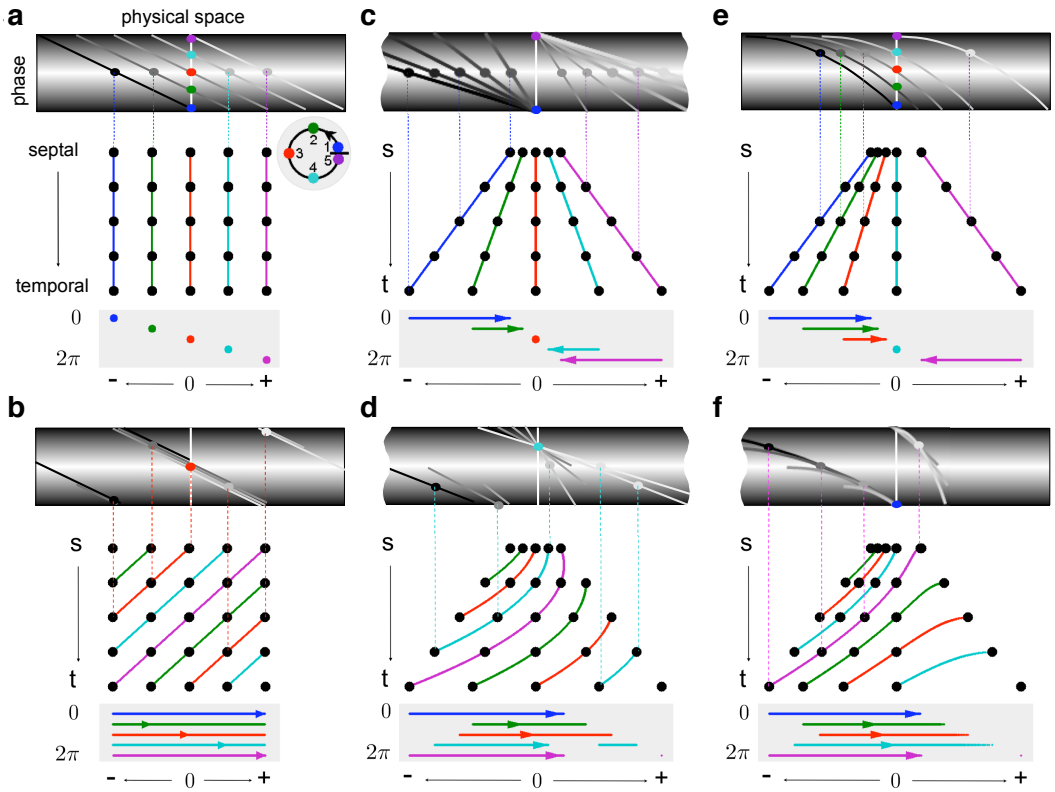

FIGURE S 17: **Hippocampal representation of physical space.** Panels illustrate representations constructed under different assumptions for a rat running on a linear track from left to right: top row (a, c, e) - synchronous theta oscillations; bottom row (b, d, f) - traveling theta waves; 1^{st} column (a, b) - equal place fields, linear precession; 2^{nd} (c, d) - field increase, linear precession; 3^{rd} (e, f) - field increase, non-linear precession; **(a) top** Gray lines show phase precession relations with respect to theta oscillations at the septal pole for place fields overlapping the rat's location. Gray dots mark place field centers. The identity of neurons that fire at 5 consecutive theta phases (circular inset below) is determined by the intersections (color dots) between the rat's location (white vertical line) and the precession curves (gray lines). Moving from the blue to the magenta time points, the field centers of the active cells advance in physical space. **middle** The same construction applies to every septotemporal level (y-axis) and, when place fields are of equal size throughout, yields a rectangular grid of field centers (black dots). Lines connect the field centers of co-active neurons at different time points (colors). The lines are vertical, because theta is in phase throughout the long axis and so is the advance of active field centers with time. **bottom** Projecting the color lines to the x-axis gives the range of physical space represented at each time. Here the hippocampus represents points of physical space at each instant. **(b)** Same as (a), but for traveling waves with wavelength equal to the long axis. **top** The increasing theta phase offsets along the long axis produce corresponding circular offsets in the precession relations computed with respect to a single theta reference (notice wraparound). **middle** Accordingly, the lines connecting the field centers of co-active cells are forward slanted. **bottom** Here a segment of physical space is topographically mapped on the long axis. Arrows mark the physical location represented at the septal pole. **(c)** Same as (a), but for a systematic 5-fold increase of place field sizes along the long axis. **top** The precession relations exhibit a range of slopes. **middle** Consequently, the rectangular grid of field centers in (a) is rescaled into a pyramid, but the rest of the derivation is the same. **bottom** In this case, the hippocampus can represent segments even in the absence of traveling waves, but their length and orientation depend on the phase of theta. **(d)** With traveling waves, the segments are of consistent length and orientation throughout (d bottom). **(e,f)** When phase precession is non-linear, the advance of active field centers with time is non-linear, and so the black dots on each row of the pyramid in (c, d) are unequally spaced. The rest of the derivation and the conclusions are the same.

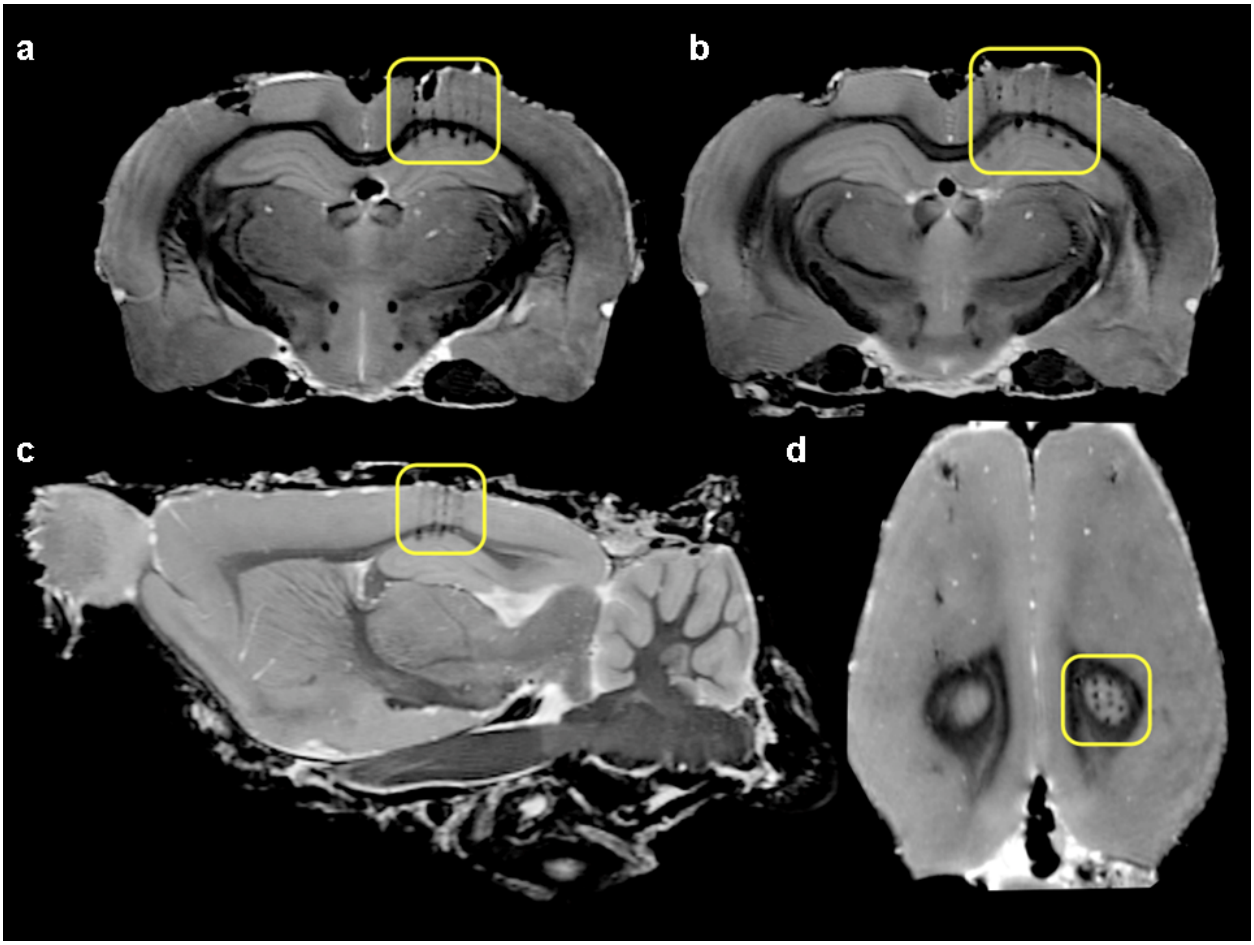

FIGURE S 18: **High resolution MRI electrode track visualization. (a-b)** Coronal, **(c)** sagittal, and **(d)** horizontal sections through the 3D MRI scan of the fixed brain of the rat implanted with the 4x8 grid. Small lesion holes mark the tetrode tip locations (d). Tetrode tracks leading to the lesion holes can also discerned (a-c). Notice the rectangular geometric arrangement of the tracks, showing that electrodes reached their targets successfully.

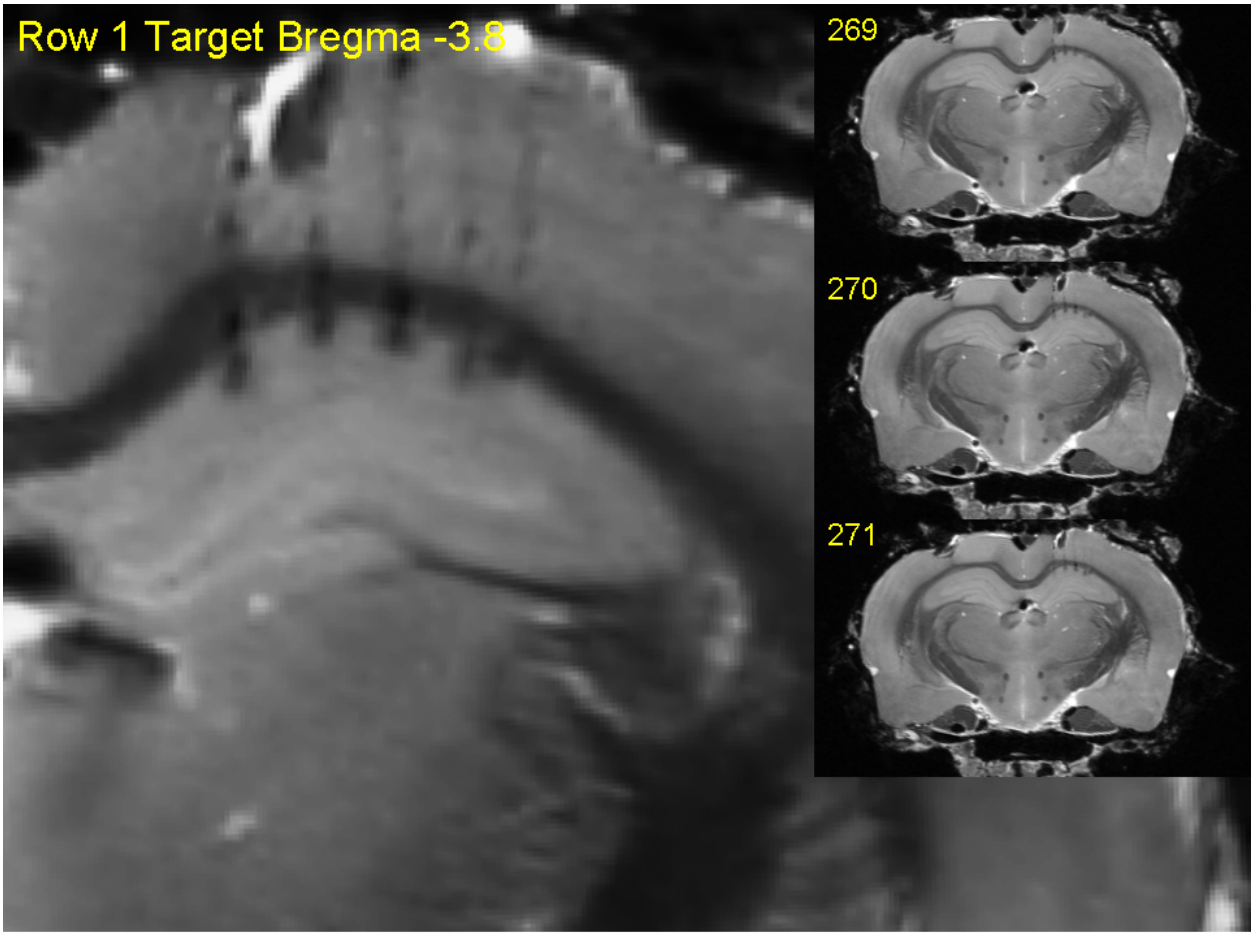

FIGURE S 19: **MRI coronal section (raw data): 4x8 grid row 1**

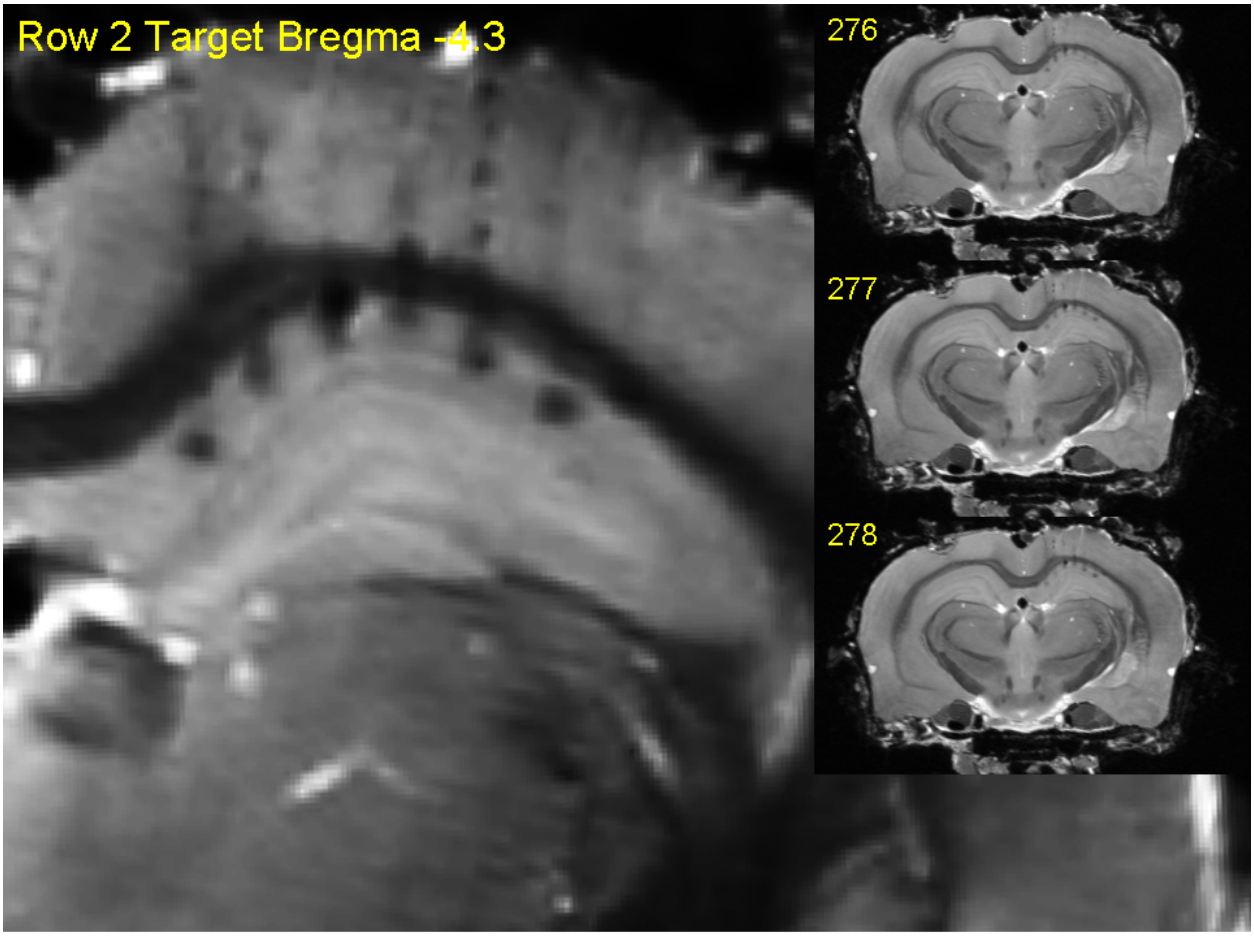

FIGURE S 20: **MRI coronal section (raw data): 4x8 grid row 2**

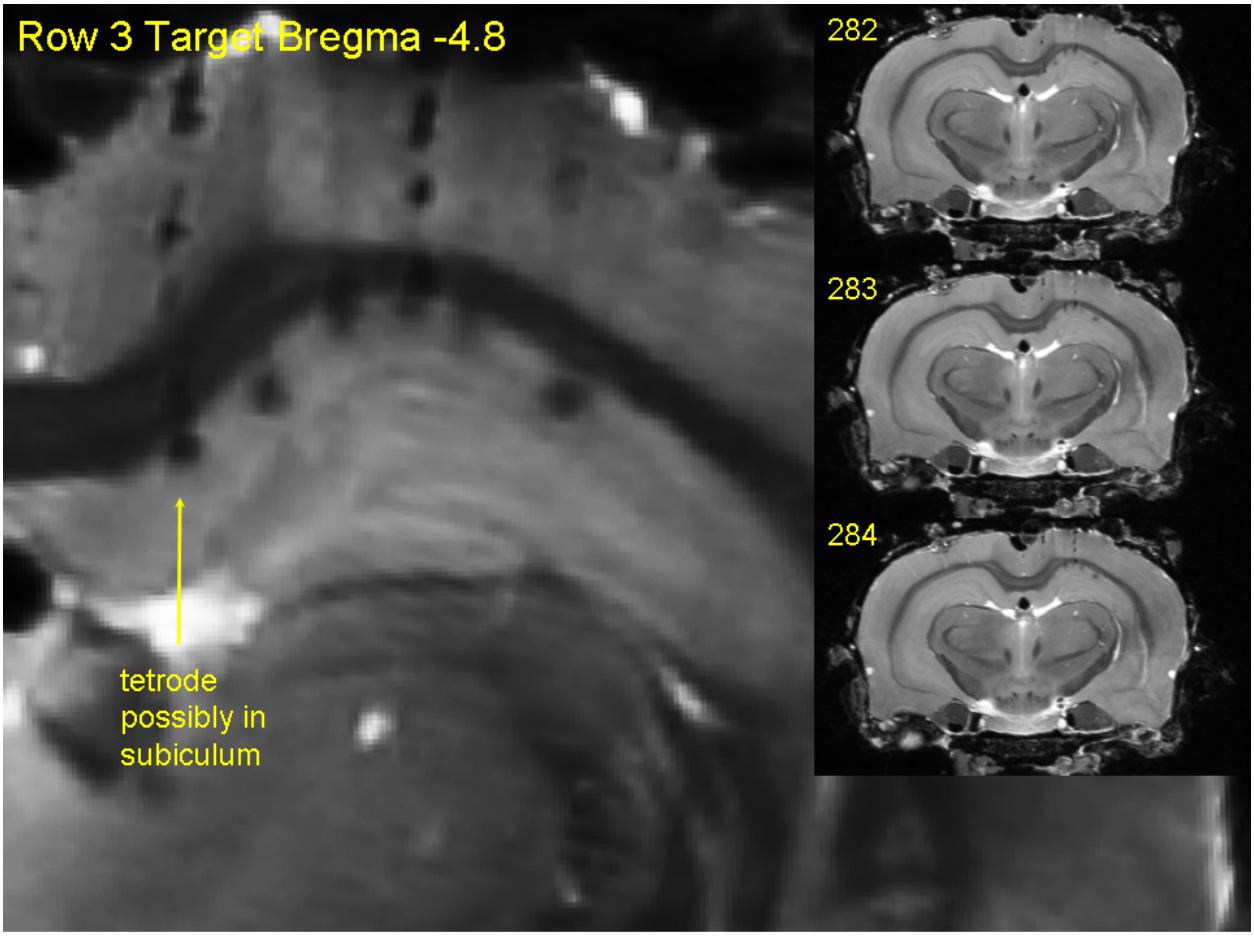

FIGURE S 21: **MRI coronal section (raw data): 4x8 grid row 3**

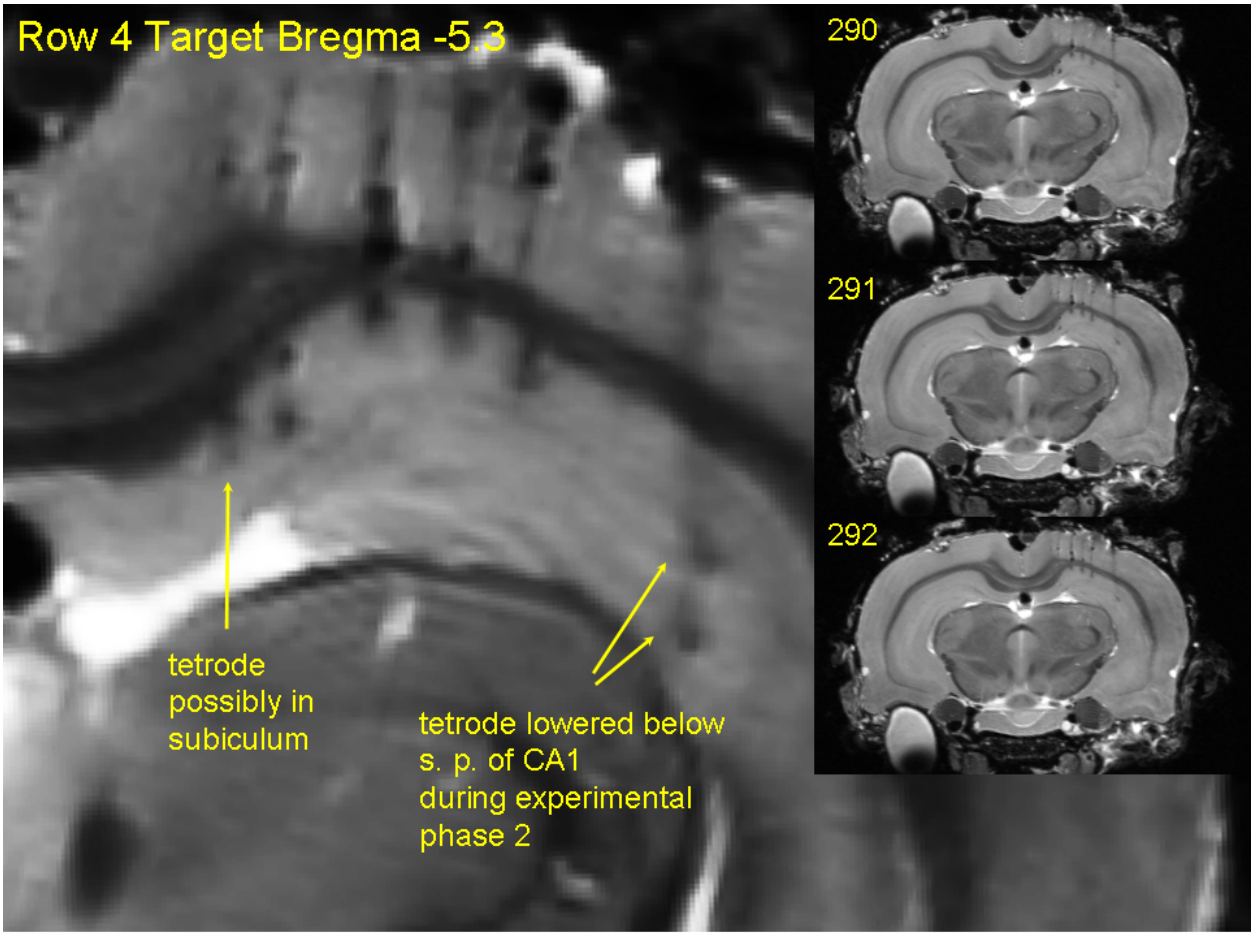

FIGURE S 22: **MRI coronal section (raw data): 4x8 grid row 4**

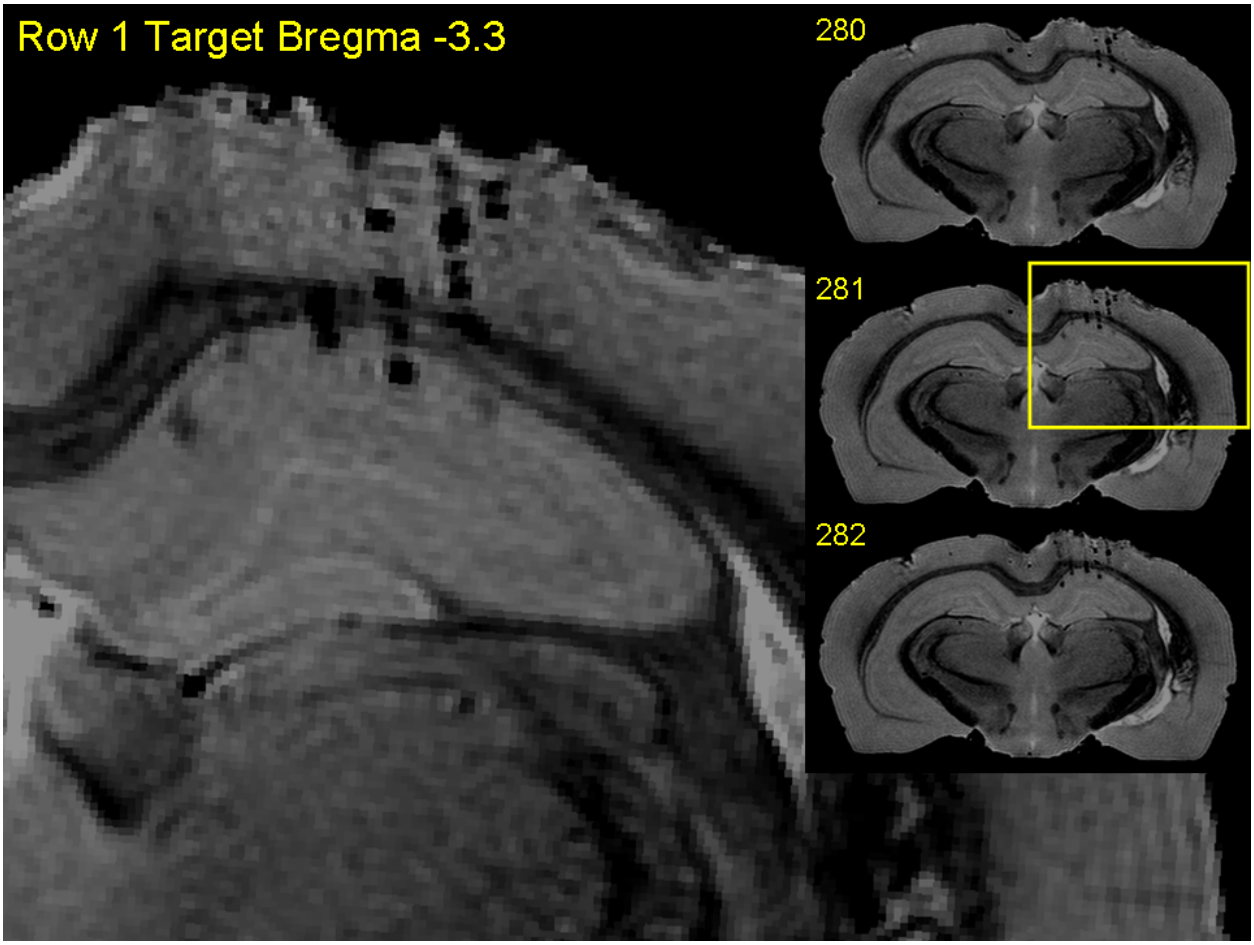

FIGURE S 23: **MRI coronal section (raw data): 5x6 grid row 1**

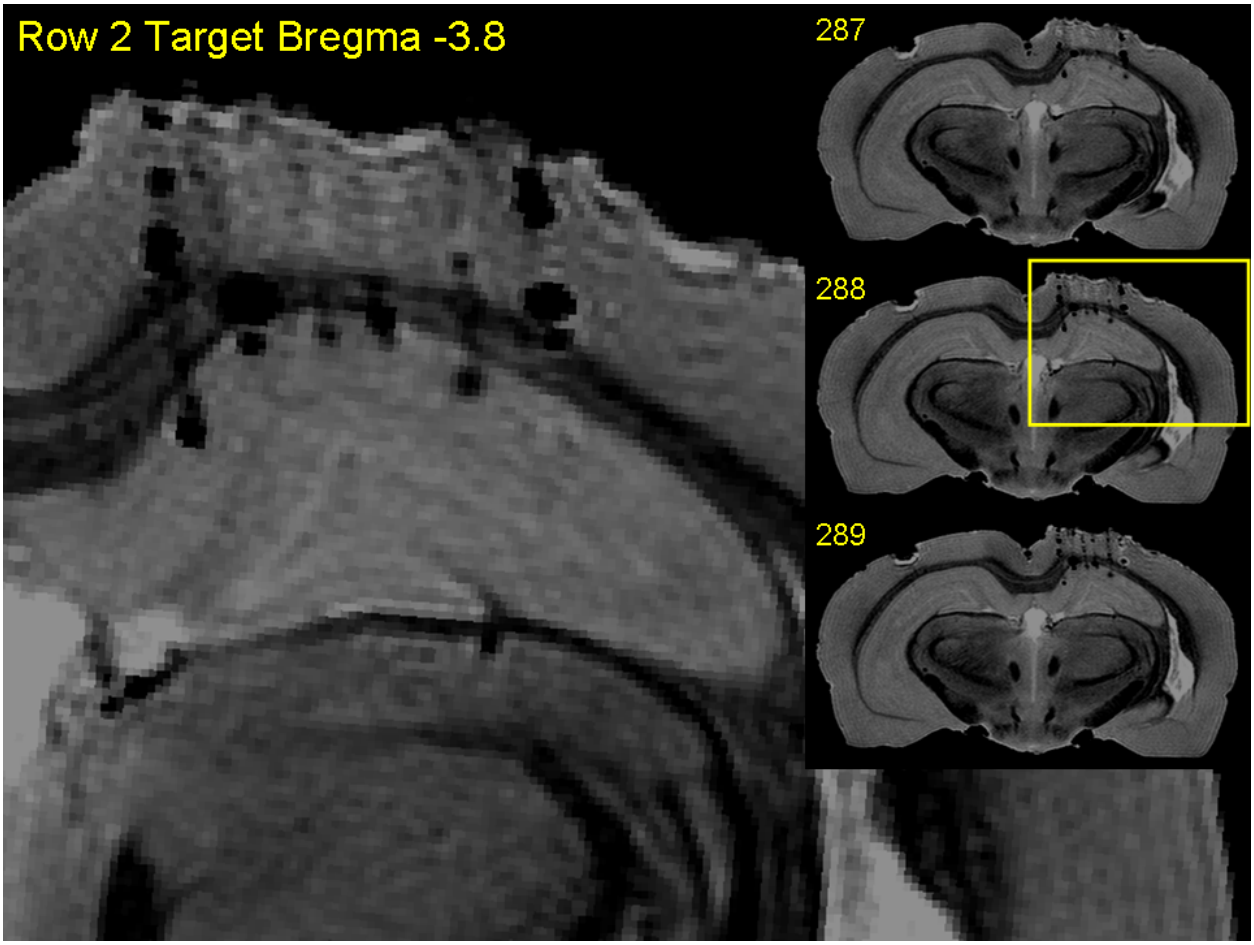

FIGURE S 24: **MRI coronal section (raw data): 5x6 grid row 2**

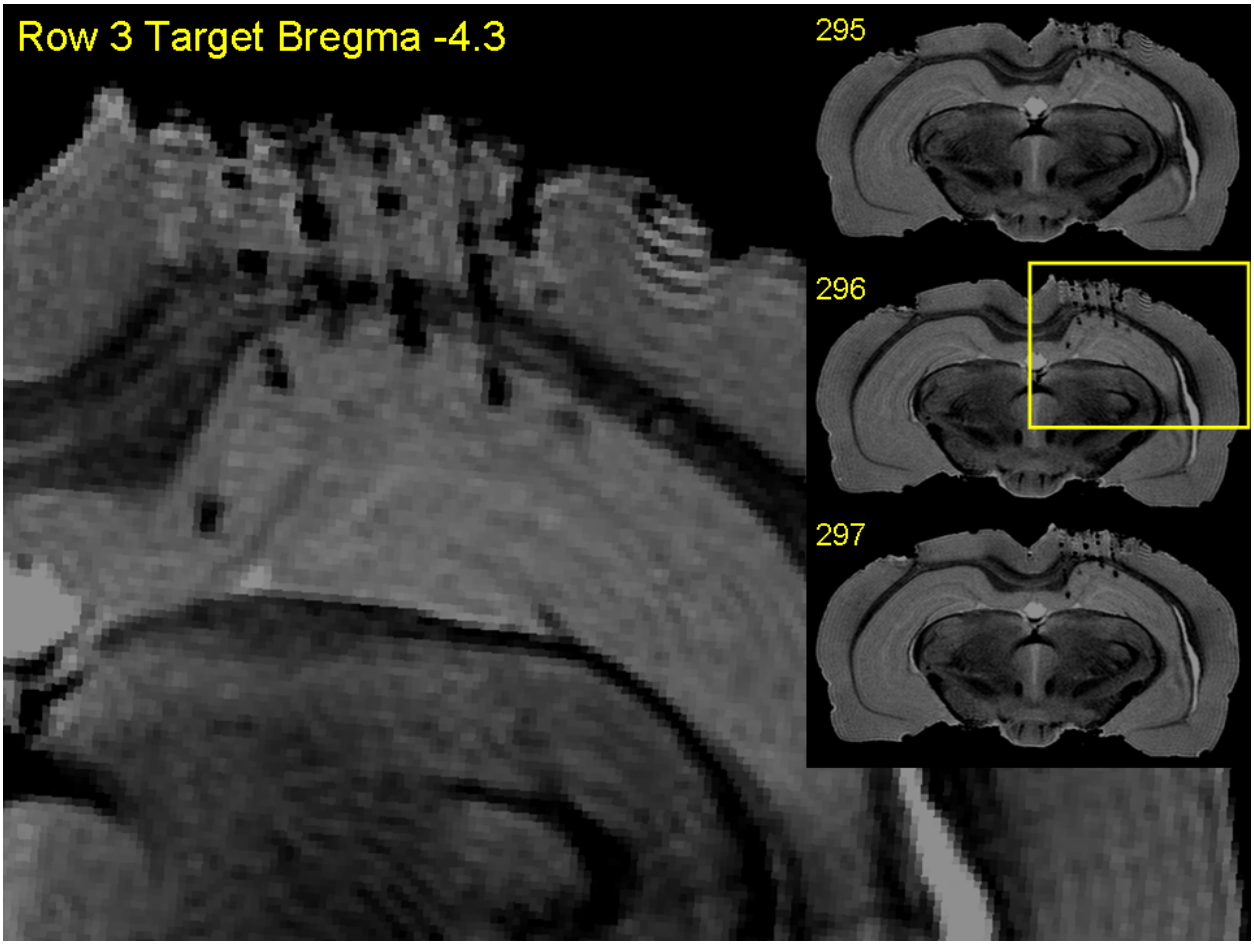

FIGURE S 25: **MRI coronal section (raw data): 5x6 grid row 3**

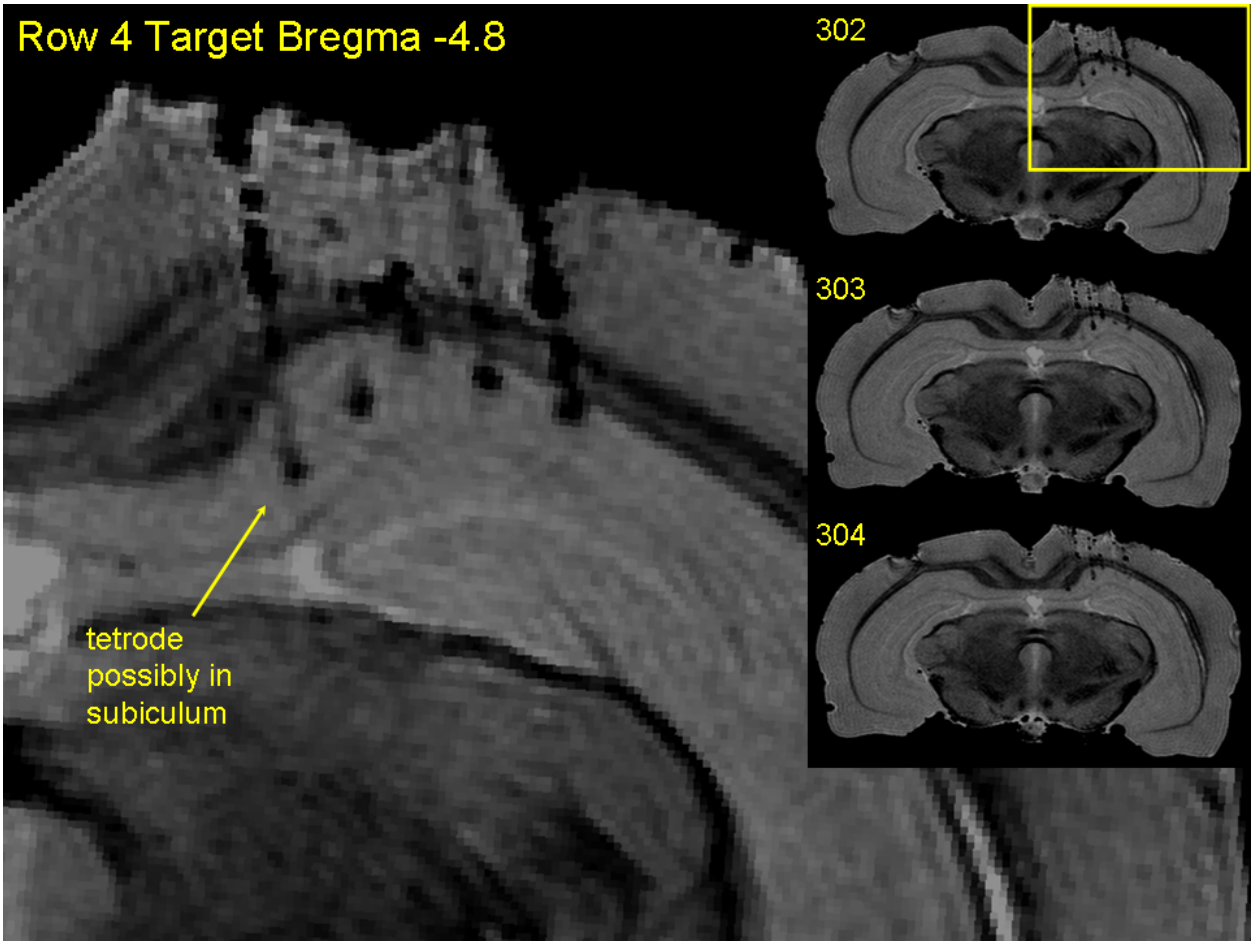

FIGURE S 26: **MRI coronal section (raw data): 5x6 grid row 4**

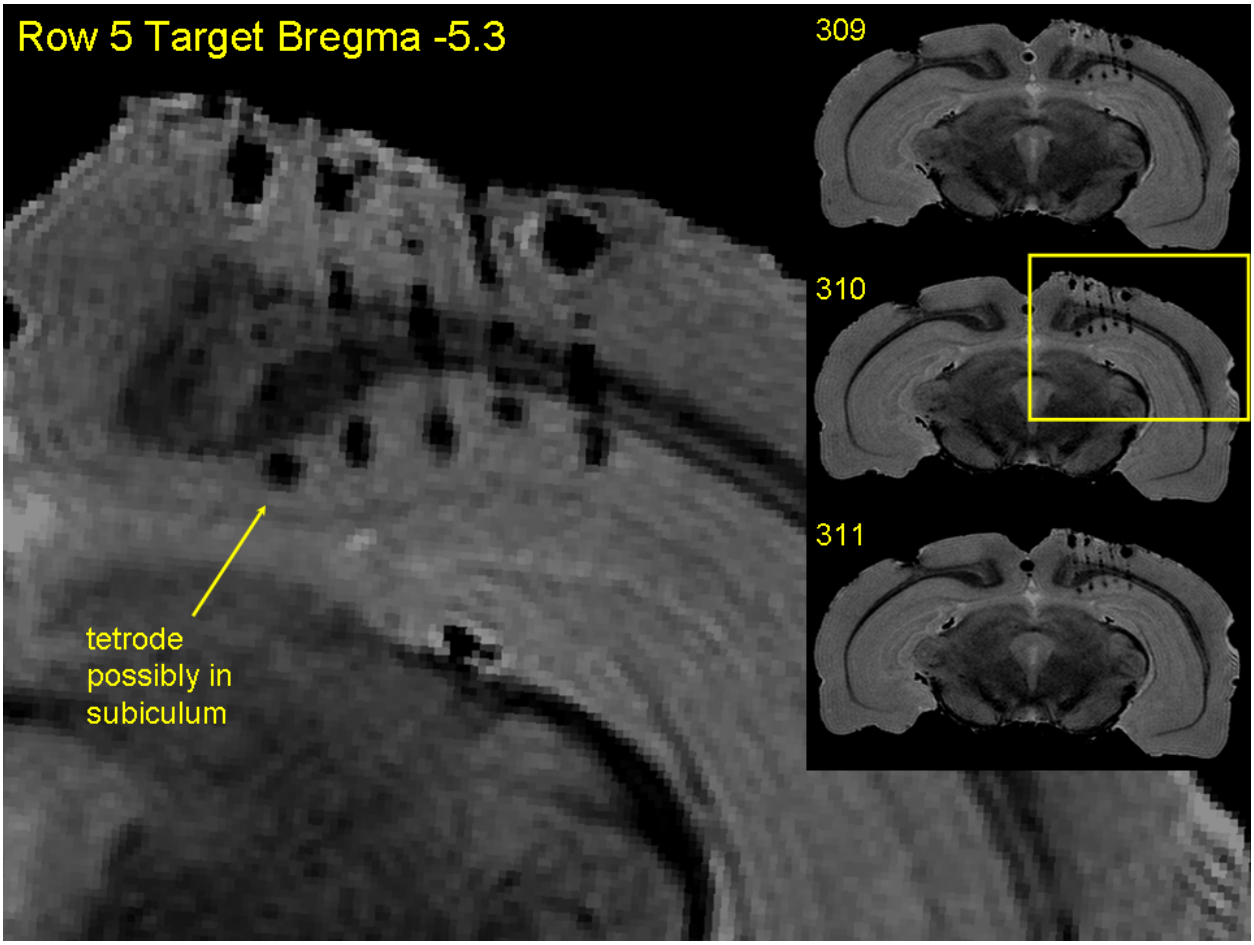

FIGURE S 27: **MRI coronal section (raw data): 5x6 grid row 5**